SIAM J. Applied Dynamical Systems
Vol. 14, No. 2, pp. 1130–1164

A Degenerate 2:3 Resonant Hopf–Hopf Bifurcation as Organizing Center of the Dynamics: Numerical Semiglobal Results*

G. Revel†, D. M. Alonso†, and J. L. Moiola†

Abstract. In this paper a degenerate case of a 2:3 resonant Hopf–Hopf bifurcation is studied. This codimension-four bifurcation occurs when the frequencies of both Hopf bifurcation branches have the relation 2/3, and one of them presents the vanishing of the first Lyapunov coefficient. The bifurcation is analyzed by means of numerical two- and three-parameter bifurcation diagrams. The two-parameter bifurcation diagrams reveal the interaction of cyclic-fold, period-doubling (or flip), and Neimark–Sacker bifurcations. A nontrivial bifurcation structure is detected in the main three-parameter space. It is characterized by a fold-flip (FF) bubble interacting with curves of fold-Neimark–Sacker (FNS), generalized period-doubling (GPD), 1:2 strong resonances ($R_{1:2}$), 1:1 strong resonances of period-two cycles ($R_{1:1}^{(2)}$), and Chenciner bifurcations (CH). Two codimension-three points with nontrivial Floquet multipliers $(1,-1,-1)$, where the bifurcation curves FF, FNS, $R_{1:2}$, and CH interact, are detected. A second pair of codimension-three points appears when FF interacts with GPD and $R_{1:1}^{(2)}$ (and CH in one of the points). Finally, it is shown that this degenerate 2:3 resonant Hopf–Hopf bifurcation acts as an organizing center of the dynamics, since the structure of bifurcation curves and its singular points are unfolded by this singularity.

Key words. Hopf–Hopf bifurcation, strong resonances, nonlinear autonomous oscillators

AMS subject classifications. 24C23, 34C15, 34C60, 37G15, 65L07

DOI. 10.1137/140968197

1. Introduction.

The Hopf–Hopf bifurcation of equilibrium points explains the origin of a class of interactions between oscillatory modes in autonomous nonlinear dynamical systems. This bifurcation is characterized by the transversal intersection of two Hopf bifurcation branches in the parameter space. At this point the linearized system has two pairs of pure imaginary eigenvalues $\pm i\omega_1$ and $\pm i\omega_2$. When the ratio of frequencies ω_1/ω_2 is irrational, the dynamics can be described by a two-dimensional (2D) truncated normal form, also known as the amplitude system, since the amplitudes of the orbits are decoupled from their phases. In these cases, the periodic orbits emerging at each Hopf bifurcation branch (with frequencies ω_1 and ω_2, respectively) can undergo Neimark–Sacker bifurcations, generating quasi-periodic orbits (2D tori). Therefore, in addition to the pair of Hopf branches, the canonical unfolding of the truncated normal form of this codimension-two bifurcation always includes two Neimark–Sacker bifurcation curves. In special cases, two additional bifurcation curves appear, and a three-dimensional (3D) torus arises [18]. When the ratio of frequencies is rational, i.e.,

*Received by the editors May 7, 2014; accepted for publication (in revised form) by H. Osinga April 15, 2015; published electronically June 24, 2015. This work was supported by Universidad Nacional del Sur (PGI 24/K052), CONICET (PIP-112-201201-00144), and ANPCyT (PICT-2010-0465).
http://www.siam.org/journals/siads/14-2/96819.html
†Instituto de Investigaciones en Ingeniería Eléctrica "Alfredo Desages" (UNS-CONICET), Departamento de Ingeniería Eléctrica y de Computadoras, Universidad Nacional del Sur, Bahía Blanca, Buenos Aires 8000, Argentina (grevel@uns.edu.ar, dalonso@uns.edu.ar, jmoiola@uns.edu.ar).

$\omega_1/\omega_2 = p/q$ with p and q integers, a p:q resonant Hopf–Hopf bifurcation occurs. In particular, when $p + q \leq 5$, the resonance is called strong [19]. In these cases, the 2D amplitude system is not valid (the amplitudes of the orbits cannot be decoupled from their phases) and a higher dimensional system is required to describe the dynamics. For example, the generic 1:1 resonant Hopf–Hopf bifurcation (with $\omega_1 = \omega_2 \neq 0$) is described by a 3D system (two amplitude equations and one phase equation). This codimension-three singularity can be interpreted as the origin (or end) of a branch of codimension-two nonresonant Hopf–Hopf bifurcations (with the local behavior described in [18]). In a three-parameter space, this branch is the handle of the Whitney umbrella formed by the stratified set of Hopf bifurcation points in the neighborhood of the resonance [12]. The 1:1 resonance gathers other codimension-two bifurcation curves (see [31, 29] and references therein), namely, a branch of generalized Hopf bifurcation points of the equilibrium, a branch of 1:1 strong resonant Neimark–Sacker bifurcation of limit cycles, a branch of Chenciner bifurcations of 2D torus, and a branch of fold-Neimark–Sacker bifurcations of limit cycles. These codimension-two bifurcation curves enable the occurrence of more complex interactions between periodic and quasi-periodic orbits.

In general, the structure of a codimension-n bifurcation and the associated interactions is exposed by performing semiglobal bifurcation analyses on sections of dimension $n - 1$ of the parameter space near the singularity [4]. The term semiglobal means that the dynamics is studied on a relatively large region, instead of considering an infinitesimally small one in the neighborhood of the bifurcation point. For example, two-parameter semiglobal unfoldings on sections near the 1:1 resonant Hopf–Hopf bifurcation must include some of the codimension-two phenomena listed before, and their subordinated curves of codimension-one bifurcations. Let us describe briefly the related bifurcation scenarios on 2D sections perpendicular to the handle of the Whitney umbrella (in [31], a section parallel to the handle is considered). On one hand, when the section does not intersect the handle (branch of nonresonant Hopf–Hopf bifurcations), the scenarios always include two nonintersecting Hopf bifurcation curves. Depending on the value of the parameters, the following four possible scenarios can arise, adding to the nonintersecting Hopf bifurcation curves: (i) no other bifurcations; (ii) a pair of generalized Hopf bifurcation points on each Hopf branch and the associated saddle-node bifurcations of periodic orbits (cyclic-fold bifurcation); (iii) the same as (ii) but with a Neimark–Sacker curve interacting with the cyclic-fold curves in a fold-Neimark–Sacker bifurcation point; (iv) the same as (iii) but without the generalized Hopf points, i.e., the cyclic-fold bifurcation curves are not connected to the Hopf branches. On the other hand, when the section intersects the handle of the Whitney umbrella, a nonresonant Hopf–Hopf bifurcation point is always present in the unfolding. At this singularity, two Neimark–Sacker bifurcation curves arise, and the scenario is completed with (v) no other bifurcations; (vi) a pair of generalized Hopf bifurcation points on each Hopf branch and the associated cyclic-fold curves; (vii) a structure involving the generalized Hopf bifurcation points, the associated cyclic-fold curves, and pairs of 1:1 strong resonances and Chenciner bifurcations on each Neimark–Sacker curve; (viii) the same as (vii) but without the pair of generalized Hopf points, i.e., the cyclic-fold curves are not connected to the Hopf branches. The aforementioned singularities enable the occurrence of complex interactions between periodic and quasi-periodic solutions, such as saddle-node bifurcations of tori and possibly chaotic dynamics [31]. Recently, the normal form of the 1:1 resonant Hopf–Hopf bifurcation with Huygens symmetry has been developed

in [15]. This special symmetric case unfolds a structure of bifurcation curves that, in a two-parameter section, includes two bubbles of cyclic-fold bifurcations (where phase-locking of the mixed-mode occurs) and bifurcation curves that give rise to a quasi-periodic 3D torus (called "toroidal breather"). The bubbles are connected by two cyclic-fold curves delimiting a region where two mixed-mode phase-locked oscillations coexist.

Structures of bifurcations are typically encountered in other p:q strong resonant Hopf–Hopf bifurcation cases. For example, they were observed in the numerical three-parameter unfolding of the 1:2 Hopf–Hopf bifurcation [26]. In the considered case (a simple example of an electrical oscillator), the bifurcation unfolds several codimension-two bifurcation branches, namely, a nonresonant Hopf–Hopf bifurcation curve, two 1:1 and two 1:2 strong resonant Neimark–Sacker bifurcation curves, a generalized Hopf bifurcation curve, a cusp of cyclic-fold bifurcations, and two generalized period-doubling bifurcation curves. Some of these codimension-two phenomena, in particular the degenerate period-doubling bifurcations, were observed in analytical studies [16, 21, 20]. Two-parameter slices in the neighborhood of the 1:2 resonance include the transversal Hopf branches (H_1 with frequency ω_1, and H_2 with frequency $\omega_2 \simeq 2\omega_1$) and the associated Neimark–Sacker curves (NS_1 and NS_2, respectively). In addition, a couple of 1:1 strong resonances appears on the Neimark–Sacker curve NS_1, and a couple of 1:2 strong resonances appears on the curve NS_2. The couple of 1:2 strong resonances on NS_2 is connected by a closed curve or bubble of period-doubling bifurcations with a pair of generalized period-doubling singularities. These points are connected by a cyclic-fold curve, which also interacts with the 1:1 strong resonances that appear on the Neimark–Sacker curve NS_1. The structures appearing on the Neimark–Sacker curves NS_1 and NS_2 coincide, respectively, with those observed separately in the k:1 and k:2 normal-internal resonances in quasi-periodically forced systems [4, 27]. A similar bifurcation structure has been detected in the study of the 2:3 resonant Hopf–Hopf bifurcation [25], where the scenarios corresponding to the k:2 and k:3 normal-internal [5] resonances are joined. In this case, the three-parameter unfolding includes the nonresonant Hopf–Hopf bifurcation branch, a couple of 1:2 and one 1:3 Neimark–Sacker strong resonance bifurcation curves, and two generalized period-doubling bifurcation curves. The structure associated to the couple of 1:2 strong resonances on the Neimark–Sacker branch NS_1 (associated to the Hopf branch H_1 with frequency ω_1) is similar to that described above for the 1:2 resonant Hopf–Hopf bifurcation; i.e., these points are connected by a bubble of period-doubling bifurcations, with two generalized period-doubling bifurcation points. The cyclic-fold curve emerging at the generalized period-doubling points interacts with the 1:3 strong resonance on the Neimark–Sacker branch NS_2 (associated to the Hopf branch H_2 with frequency $\omega_2 \simeq 3/2\,\omega_1$). Notice that the period-two cycle emerging at the period-doubling bubble on one side of the bifurcation structure evolves into a period-three cycle near the 1:3 strong resonance point on the opposite side (see [25] for details).

The complexity of interactions near a 2:3 resonant Hopf–Hopf bifurcation increases when the first Lyapunov coefficient of one of the Hopf branches passes through zero at the resonant point. Roughly speaking, the generalized Hopf bifurcation introduces a third limit cycle by means of the associated cyclic-fold curve, and this cycle interacts with the periodic and quasi-periodic orbits existing in the 2:3 resonance. This codimension-four singularity is interesting since it acts as an organizing center of the dynamics, in the sense that bifurcations of codimension-three or less are subordinated to it (this works in general for codimension-n

bifurcations [4]). In this paper, we analyze one case of the degenerate 2:3 resonant Hopf–Hopf bifurcation of the equilibrium point in a four-parameter space by performing systematic two- and three-parameter semiglobal studies near the singularity. The aim of the analysis is to give insight into the mechanism by which the degeneracy condition in one of the Hopf bifurcation branches is transferred to the Hopf–Hopf resonant (and nonresonant) scenario. In the considered case, the degenerate Hopf bifurcation condition is on the branch H_1 (with frequency ω_1), and we will show that the fold bifurcation is transferred to the structure associated to NS_1, i.e., that involving the period-doubling bubble and the pair of 1:2 strong resonances. Notice that additional local phenomena do not arise on the branch NS_2. A new structure of codimension-two bifurcation curves associated to H_1 and NS_1, resembling that observed in the two-parameter analysis of the 2:3 Hopf–Hopf bifurcation, is detected. It consists mainly in a bubble of fold-flip bifurcations, a fold-Neimark–Sacker bifurcation curve, and a couple of 1:2 strong resonances (i.e., a fold bifurcation is added to the Neimark–Sacker, the period-doubling bubble, and the cyclic-fold curves observed in the nondegenerate 2:3 Hopf–Hopf bifurcation). In the three-parameter space, the new structure of limit-cycle bifurcations is organized around four codimension-three singularities. Two of them correspond to an interaction between fold-flip bifurcations, 1:2 strong resonances, and fold-Neimark–Sacker and Chenciner bifurcations, leading to nontrivial Floquet multipliers of the limit cycle at $(1, -1, -1)$. The other two subordinate a fold-flip bifurcation, a generalized period-doubling bifurcation, and a 1:1 strong resonance of period-two cycles (one of them also generates a Chenciner bifurcation). This structure is analyzed by performing detailed two-parameter numerical semiglobal bifurcation diagrams, and the richness of the associated dynamics is shown by numerical simulations. Finally, it is shown that when the four-parameter space is considered, the degenerate 2:3 resonant Hopf–Hopf bifurcation of equilibria acts as the organizing center of the dynamics, i.e., the whole structure (the codimension-three bifurcations of limit cycles and the subordinated codimension-two curves) is unfolded by the singularity.

The rest of the paper is organized as follows. In section 2, the equations of the oscillator used as an example are introduced and are generalized as two second order coupled subsystems. A general description of the Hopf–Hopf bifurcation and its resonances is also given. In section 3, two-parameter semiglobal bifurcation analyses near the degenerate 2:3 Hopf–Hopf bifurcation are performed. A three-parameter numerical semiglobal unfolding is carried out in section 4, and the structure involving the fold-flip bubble, fold-Neimark–Sacker, strong resonances, generalized period-doubling, and Chenciner bifurcations curves is analyzed in section 5. In section 6, the role of the degenerate 2:3 resonant Hopf–Hopf bifurcation as a codimension-four organizing center of the dynamics is discussed. Finally, in section 7 some conclusions are included.

2. Hopf–Hopf bifurcation on a model of a simple electrical oscillator. We consider a four-dimensional (4D) dynamical system modeling a simple electrical oscillator. The interest in using this circuit as a benchmark for studying the Hopf–Hopf bifurcation is that different unfoldings and relevant p:q resonances can be created by varying physical parameters. The circuit has been used by the authors to investigate the 2:3 and 1:2 resonant cases in [25, 26], respectively. In this section, the attention is focused on presenting the model and highlighting

some structural properties rather than describing its physical features. The model is given by

$$
\begin{aligned}
\dot{x}_1 &= \eta_1 \left(\alpha_1 x_1 + x_2 - x_4 - \alpha_2 x_1^2 - \alpha_3 x_1^3\right), \\
\dot{x}_2 &= -\eta_3 x_1, \\
\dot{x}_3 &= \rho_1 x_4, \\
\dot{x}_4 &= \rho_2 \left(x_1 - x_3 - \eta_2 x_4\right),
\end{aligned} \tag{1}
$$

where x_i, $i = 1, 2, 3, 4$, are the state variables; η_1, η_2, and η_3 are the main bifurcation parameters; ρ_1 and ρ_2 are constant parameters; and α_1, α_2, and α_3 are auxiliary parameters. All of the parameters are positive and are univocally related to the physical parameters of the circuit (see [25, 26] for details).

2.1. A more general representation. The model (1) can be represented as two second order coupled subsystems by considering the coordinates $(y_1, y_2) = (\omega_{n_2}/\eta_3\, x_2, x_3)$, resulting in

$$\ddot{y}_1 - \sigma_1 \left[1 - f(\dot{y}_1)\right] \dot{y}_1 + \omega_{n_1}^2 y_1 - \sigma_{12} \dot{y}_2 = 0, \tag{2}$$

$$\ddot{y}_2 + \sigma_2 \dot{y}_2 + \omega_{n_2}^2 y_2 + \omega_{n_2} \dot{y}_1 = 0. \tag{3}$$

The primary subsystem (2) is basically a self-excited nonlinear oscillator, similar to the Rayleigh one, with a self-excitation coefficient $\sigma_1 = \eta_1 \alpha_1$, a nonlinear coefficient $f(\dot{y}_1) = \left(-\alpha_2 \dot{y}_1/\omega_{n_2} + \alpha_3 \dot{y}_1^2/\omega_{n_2}^2\right)/\alpha_1$, a natural frequency $\omega_{n_1} = \sqrt{\eta_1 \eta_3}$, and a "velocity" coupling term $\sigma_{12}\dot{y}_2$ with $\sigma_{12} = \eta_1 \omega_{n_2}/\rho_1$. The secondary subsystem (3) is a damped linear oscillator (or load) with damping coefficient $\sigma_2 = \eta_2 \rho_2$, a natural frequency $\omega_{n_2} = \sqrt{\rho_1 \rho_2}$, and a coupling term $\omega_{n_2}\dot{y}_1$. In this paper, ρ_1 and ρ_2 are fixed at $\rho_1 = 1 + \sqrt{2}$ and $\rho_2 = 2 - \sqrt{2}$. Thus, the natural frequency of the secondary subsystem (3) is fixed at $\omega_{n_2} = 2^{1/4} = 1.1892$. In addition, the auxiliary parameter α_3 is fixed at $\alpha_3 = 1$.

The representation (2)–(3), although simple, is more general than (1) and places the results derived here in the context of coupled second order systems. Interacting second order systems are frequently used to describe several problems in engineering and physics. Simple self-excited systems with linear couplings are treated in [24], and with nonlinear couplings in [1, 33, 3], just to mention a few.

2.2. Hopf–Hopf bifurcation condition. The defining conditions of the Hopf–Hopf bifurcation using a dimensionless version of the system (2)–(3) are derived in Appendix A. These conditions determine that (i) the self-excitation (linear) coefficient of subsystem (2) must be equal to the damping coefficient of subsystem (3), i.e., $\sigma_1 = \sigma_2$ (see (17)); (ii) the natural frequencies of both subsystems must be equal, i.e., $\omega_{n_1} = \omega_{n_2}$ (see (18)); (iii) the coupling coefficient $\sigma_{12} > \sigma_1\, \sigma_2$ (see (19)). Translating these conditions to the main bifurcation parameter space (η_1, η_2, η_3) results in the codimension-two Hopf–Hopf bifurcation curve (parameterized in η_3)

$$HH = \left\{ (\eta_1, \eta_2, \eta_3) : \quad \eta_1 = \frac{\rho_1 \rho_2}{\eta_3}, \quad \eta_2 = \frac{\alpha_1 \rho_1}{\eta_3}, \quad \eta_3 \geq \rho_1 \alpha_1^2 \right\}. \tag{4}$$

The bifurcation branches involved in the Hopf–Hopf singularity will be denoted as H_1 and H_2, and their frequencies as ω_1 and ω_2, respectively. The frequencies of the Hopf bifurcations

$H_{1,2}$ on the curve (4) result in (see Appendix A)

$$\omega_{1,2} = \omega_{n_2}\sqrt{\Delta \mp \sqrt{\Delta^2 - 1}}, \tag{5}$$

where $\Delta = 1 + \rho_2\left(\eta_3 - \rho_1\alpha_1^2\right)/(2\eta_3^2) \geq 1$, since $\eta_3 \geq \rho_1\alpha_1^2$ on the Hopf–Hopf bifurcation. The ratio of frequencies is

$$\frac{\omega_1}{\omega_2} = \Delta - \sqrt{\Delta^2 - 1}. \tag{6}$$

2.3. Hopf–Hopf resonances. Letting $\omega_1/\omega_2 = p/q$ in (6) and solving for Δ results in

$$\Delta = \Delta^{p:q} = \frac{p^2 + q^2}{2pq}. \tag{7}$$

Solving for η_3 results in

$$\eta_3^{p:q\pm} = \frac{2\rho_1\alpha_1^2}{1 \pm \sqrt{1 - \left(\alpha_1/\alpha_{1c}^{p:q}\right)^2}}, \tag{8}$$

where $\alpha_{1c}^{p:q} = \sqrt{\rho_2\, p\, q/4\rho_1}/\left(p - q\right)$ and $\alpha_1 < \alpha_{1c}^{p:q}$. Notice that α_{1c} places an upper limit on the value of α_1 for the existence of p:q resonances.

Therefore, in the main bifurcation parameter space, the p:q resonant Hopf–Hopf bifurcation point results in

$$HH_{p:q}^{\pm} = \left\{(\eta_1, \eta_2, \eta_3) : \quad \eta_1 = \frac{\rho_1\rho_2}{\eta_3^{p:q\pm}}, \quad \eta_2 = \frac{\alpha_1\rho_1}{\eta_3^{p:q\pm}}, \quad \eta_3 = \eta_3^{p:q\pm}\right\}, \tag{9}$$

and the frequencies corresponding to the branches H_1 and H_2 at the singularity are

$$\omega_1^{p:q} = \omega_{n_2}\sqrt{p/q}, \quad \omega_2^{p:q} = \omega_{n_2}\sqrt{q/p}. \tag{10}$$

The values of ω_1 and ω_2 on the Hopf–Hopf bifurcation curve (4), for $\alpha_1 = 1/2$ and $\alpha_1 = 1/7$, are depicted in Figure 1(a), and the ratio ω_1/ω_2 for the same values of parameter α_1 is shown in Figure 1(b). In the latter, the horizontal dashed lines denote the five $p : q$ resonant cases with $p + q \leq 5$. In particular, the 1:1 resonance occurs at

$$HH_{1:1}^{+} = \left\{(\eta_1, \eta_2, \eta_3) : \eta_1 = \frac{\rho_1\rho_2}{\eta_3^{1:1+}}, \quad \eta_2 = \frac{\alpha_1\rho_1}{\eta_3^{1:1+}}, \quad \eta_3 = \eta_3^{1:1+} = \rho_1\alpha_1^2\right\}. \tag{11}$$

In the main parameter space (η_1, η_2, η_3), the resonance point can be interpreted as the beginning of the Hopf–Hopf bifurcation curve (4), and it exists for any value of α_1 (since $\alpha_{1c}^{1:1} \to \infty$). The curve ends in a second 1:1 resonance for $\eta_3 = \eta_3^{1:1-} \to \infty$, i.e., at $HH_{1:1}^{-} = (0, 0, \infty)$. The corresponding frequencies are $\omega_1^{1:1} = \omega_2^{1:1} = \omega_{n_2} = 2^{\frac{1}{4}}$.

As noted above, and denoted in Figure 1(b), the value of parameter α_1 plays a critical role in the existence of additional p:q resonances on the Hopf–Hopf bifurcation curve (4). In

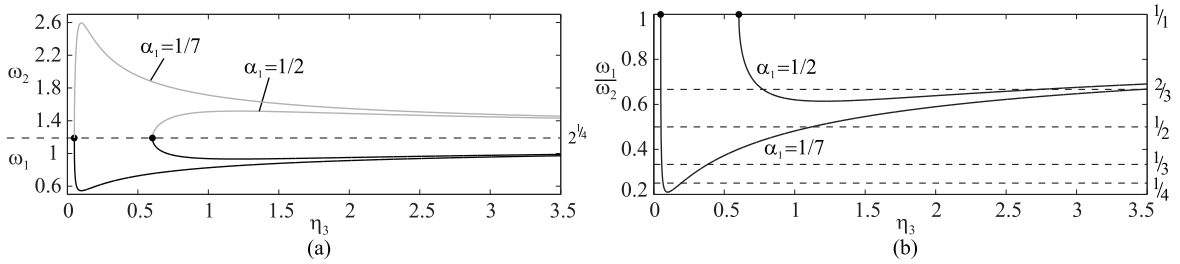

Figure 1. *Frequencies of Hopf branches H_1 and H_2 associated with the Hopf–Hopf bifurcation.* (a) *Frequencies ω_1 (black) and ω_2 (gray) varying η_3 for $\alpha_1 = 1/2$ and $\alpha_1 = 1/7$.* (b) *Frequency ratio ω_1/ω_2.*

particular, for $\alpha_1 < \alpha_{1c}^{2:3}$, with $\alpha_{1c}^{2:3} = \sqrt{3/2}\sqrt{\rho_2/\rho_1} \simeq 0.6033$, a pair of 2:3 resonant points occurs at

$$HH_{2:3}^{\pm} = \left\{ (\eta_1, \eta_2, \eta_3) : \eta_1 = \frac{\rho_1\rho_2}{\eta_3^{2:3\pm}}, \quad \eta_2 = \frac{\alpha_1\rho_1}{\eta_3^{2:3\pm}}, \quad \eta_3 = \eta_3^{2:3\pm} = \frac{2\rho_1\alpha_1^2}{1 \pm \sqrt{1 - \frac{2\rho_1\alpha_1^2}{3\rho_2}}} \right\}. \tag{12}$$

The corresponding frequencies are $\omega_1^{2:3} = \omega_{n_2}\sqrt{2/3} \simeq 0.9710$ and $\omega_2^{2:3} = \omega_{n_2}\sqrt{3/2} \simeq 1.4565$. The 2:3 resonant Hopf–Hopf singularity generates a structure of bifurcations involving 1:2 and 1:3 Neimark–Sacker strong resonances, a period-doubling bubble, cyclic folds, and degeneracy points as described in [25]. Since the focus of the analysis is the degenerate case of the 2:3 resonant Hopf–Hopf bifurcation, the auxiliary parameter α_1 is fixed at $\alpha_1 = 0.5$ such that only 1:1 and 2:3 strong resonances can appear, i.e., 1:2, 1:3, and 1:4 resonances are avoided (see Figure 1(b)). For $\alpha_1 = 0.5$, according to (11) and (12) with $\rho_1 = 1+\sqrt{2}$ and $\rho_2 = 2-\sqrt{2}$, the 1:1 and 2:3 resonances occur at the points

$$\begin{aligned}
HH_{1:1}^{+} &\simeq (2.343146, 2, 0.603553),\\
HH_{1:1}^{-} &= (0, 0, \infty),\\
HH_{2:3}^{+} &\simeq (1.827140, 1.559570, 0.774002),\\
HH_{2:3}^{-} &\simeq (0.516001, 0.440435, 2.740720).
\end{aligned}$$

The projections of the Hopf–Hopf bifurcation curve (4) on the planes (η_1, η_2) and (η_2, η_3) are depicted in Figures 2(a) and 2(b), respectively. In this paper, the analysis of $HH_{2:3}^{+}$ is considered, and for simplicity the sign is dropped, and we refer to this point as $HH_{2:3}$ in the following. The same holds with $HH_{1:1}$.

2.4. Local unfoldings for the nonresonant cases. The dynamics of (1) in the neighborhood of the equilibrium point, for parameter values sufficiently close to the Hopf–Hopf curve (excluding the transition points and resonances), can be classified in four qualitatively different local unfoldings, depending on the value of α_2. In accordance with the nomenclature used in [18], these scenarios are referred to as S.I, S.II, S.III, and D.VI, as denoted in Figure 2 for $\alpha_2 = 0.83$ (the points where the unfoldings change are denoted by empty circles). Cases S.I–S.III are called "simple" since the transversal intersection of both Hopf bifurcation branches only develops a pair of Neimark–Sacker bifurcation curves leading to 2D tori. On the other

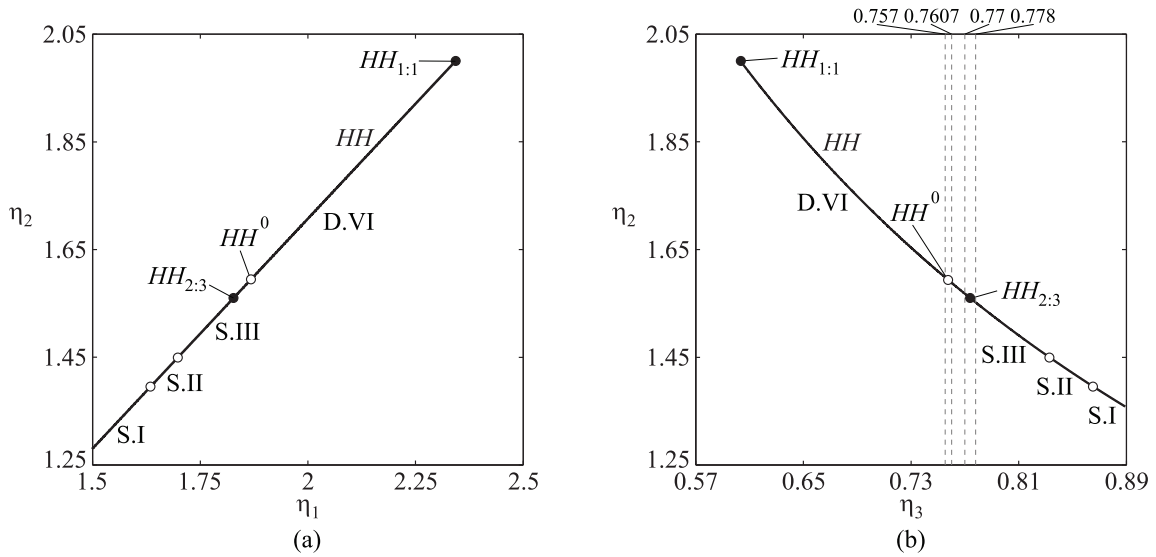

Figure 2. *Projections of the Hopf–Hopf bifurcation curve for $\alpha_1 = 1/2$ on the parameter planes.* (a) $\eta_1 - \eta_2$, (b) $\eta_2 - \eta_3$. *Resonant points $HH_{1:1}$ and $HH_{2:3}$ are denoted by black circles. The local unfoldings for $\alpha_2 = 0.83$ are indicated as S.I, S.II, and S.III (simple), and D.VI (difficult), and the transitions by empty circles.*

hand, the case D.VI is called "difficult" since it unfolds two additional bifurcation curves leading to a 3D torus. The normal form of the Hopf–Hopf bifurcation and the local unfolding of the four cases are included in Appendix B (see [18] for a detailed description). Notice that the canonical diagrams shown in Figure 19 (rotated clockwise 135°) are qualitatively equivalent to the diagrams observed in the parameter plane $\eta_1 - \eta_2$ near the Hopf–Hopf bifurcation curve.

The transition from the simple case S.III to the difficult case D.VI occurs at the point denoted as HH^0 in Figure 2. This is a codimension-three singularity where, in addition to the Hopf–Hopf bifurcation condition occurring, the first Lyapunov coefficient of the Hopf bifurcation H_1 vanishes. Increasing α_2, HH^0 approaches the 2:3 resonance $HH_{2:3}$, and for $\alpha_2 \simeq 0.86$ both points coincide, leading to a codimension-four bifurcation, denoted in the following as $HH^0_{2:3}$. This degenerate 2:3 resonance point acts as an organizing center of the dynamics, unfolding nontrivial phenomena that will be studied in the following by means of two-, three-, and four-parameter analysis. All of the bifurcations detected in this paper, with their corresponding acronyms, codimensions, critical eigenvalues or multipliers, and subordinate bifurcations, are listed in Tables 1 and 2 for equilibrium points and limit cycles, respectively.

3. Numerical two-parameter semiglobal unfoldings of the Hopf–Hopf bifurcation near the degenerate 2:3 resonant condition. As depicted in Figure 2, for $\alpha_2 = 0.83$, the degenerate Hopf–Hopf point HH^0 is close to the 2:3 resonance $HH_{2:3}$ (they coincide for $\alpha_2 \simeq 0.86$). Therefore, performing semiglobal unfoldings of the Hopf–Hopf bifurcation, useful information about the interaction of these singularities is obtained. Moreover, they can be interpreted as slices of the unfoldings of HH^0, $HH_{2:3}$, and the additional singularities arising at the interaction of the former ones. Towards this end, numerical unfoldings in the parameter plane

Table 1

Local bifurcations of equilibria detected in this paper. The fifth column (incidence) contains the subordinate bifurcations (see the acronyms of limit cycle bifurcations in Table 2). The difference between the simple and difficult cases in the Hopf–Hopf bifurcation is not indicated since the bifurcations leading to the 3D torus are not detected. The supra-indices a,b denote that two bifurcations are unfolded. The last column indicates when the normal form of the Hopf bifurcation branch H_1 is degenerate, i.e., when the first Lyapunov coefficient vanishes.

Label	Bifurcation	Codim.	Eigenvalues	Incidence (detected)	Deg. on H_1
H	Hopf	1	$\lambda_{1,2} = \pm i\omega$	-	No
GH	Bautin or generalized Hopf	2	$\lambda_{1,2} = \pm i\omega$	$H + CF$	Yes
HH	Hopf–Hopf	2	$\lambda_{1,2} = \pm i\omega_1$	$H_{1,2} + NS_{1,2}$	No
			$\lambda_{3,4} = \pm i\omega_2$		
HH^0	Degenerate Hopf–Hopf	3	$\lambda_{1,2} = \pm i\omega_1$	$HH + FNS + GH$	Yes
			$\lambda_{3,4} = \pm i\omega_2$		
$HH_{1:1}$	1:1 resonant Hopf–Hopf	3	$\lambda_{1,2} = \pm i\omega_1$	$HH + FNS + GH$	Yes
			$\lambda_{3,4} = \pm i\omega_1$		
$HH_{2:3}$	2:3 resonant Hopf–Hopf	3	$\lambda_{1,2} = \pm i\omega_1$	$HH + R^{a,b}_{1:2} + GPD^{a,b} + R_{1:3}$	No
			$\lambda_{3,4} = \pm i\frac{3}{2}\omega_1$		
$HH^0_{2:3}$	Deg. 2:3 resonant Hopf–Hopf	4	$\lambda_{1,2} = \pm i\omega_1$	$HH_{2:3} + HH^0 + Q^{a,b} + P^{a,b}$	Yes
			$\lambda_{3,4} = \pm i\frac{3}{2}\omega_1$		

$\eta_1 - \eta_2$ for $\alpha_2 = 0.83$ and four different values of η_3 (denoted as vertical dashed lines in Figure 2(b)) are performed. The two-parameter bifurcation diagrams obtained with Matcont [9] are described in the following subsections. The coefficients of the truncated normal form (29)–(30) of the Hopf–Hopf bifurcation for each case are listed in Table 3. The normal form coefficients for all of the detected bifurcations are also computed with Matcont (see [10]).

3.1. Two-parameter slice at the right of $HH_{2:3}$ ($\eta_3 = 0.778$). The numerical semiglobal unfolding of the Hopf–Hopf bifurcation in the parameter plane $\eta_1 - \eta_2$ for $\eta_3 = 0.778$ (the vertical rightmost slice in Figure 2(b)) is shown in Figure 3. Computing the coefficients of the normal form (first row of Table 3) reveals that the Hopf–Hopf bifurcation corresponds to the simple case S.III (compare Figure 3 with case S.III in Figure 19). The unfolding contains two Neimark–Sacker bifurcation curves NS^a_1 and NS^a_2 associated to the cycles born at the Hopf curves H_1 and H_2, respectively. The cyclic-fold bifurcation CF is not unfolded by the Hopf–Hopf bifurcation HH, but, as will be shown later, it arises in a generalized Hopf bifurcation of the branch H_1 and will interact with the bifurcation curves associated to HH. The superscript in $NS^a_{1,2}$ denotes that the branch begins at the Hopf–Hopf bifurcation. When parameter η_3 is varied, Neimark–Sacker strong resonances appear on these branches, and the superscript b will be used to denote the segment that evolves from the resonance point.

The limit sets corresponding to each region of the bifurcation diagram are illustrated in Figure 4. The figure shows, in the second and third rows, the projections of the orbits on the phase plane $x_1 - x_2$, and in the first and last rows, the projections on the plane $x_2 - x_3$ of the corresponding iterates at the Poincaré sections $x_1 = 0$ and $\dot{x}_1 > 0$. In the phase planes (second and third rows) the equilibrium point (origin) is denoted with a filled circle when stable (region 1) and an empty circle when unstable (regions 2–8). The limit cycles

Table 2

Local bifurcations of limit cycles detected in this paper. The superscript (2) *indicates a secondary bifurcation. The label* TF *in the incidences of* $R_{1:2}$ *and* CH *means a saddle-node bifurcation of torus (not included in the first column since it is not detected numerically). The subordinated bifurcations (incidence) indicated for* $R_{1:2}$ *and* FF *correspond to the more complex cases of their normal forms, and some of them may not be present (e.g.,* $NS^{(2)}$*). The last column denotes whether a degeneracy is present* (a) *on the period-doubling curve PD,* (b) *on the Neimark–Sacker curve NS, or* (c) *on the fold-flip curve FF, since the flip bifurcation PD is degenerate due to the generalized period-doubling bifurcation GPD.*

Label	Bifurcation	Codim.	Critical multipliers	Incidence	Degeneracy
CF	Cyclic-fold	1	$\mu_1 = 1$	-	No
NS	Neimark-Sacker	1	$\mu_{1,2} = e^{\pm i\theta}$	-	No
PD	Period-doubling or flip	1	$\mu_1 = -1$	-	No
GPD	Generalized PD	2	$\mu_1 = -1$	$PD + CF^{(2)}$	Yes [(a)]
CH	Chenciner	2	$\mu_{1,2} = e^{\pm i\theta}$	$NS + TF$	Yes [(b)]
$R_{1:1}$	1:1 strong resonance	2	$\mu_{1,2} = 1$	$NS + CF$	No
$R_{1:2}$	1:2 strong resonance	2	$\mu_{1,2} = -1$	$NS + PD + NS^{(2)} + TF$	No
$R_{1:3}$	1:3 strong resonance	2	$\mu_{1,2} = e^{\pm i\frac{2\pi}{3}}$	NS	No
FF	Fold-flip	2	$\mu_1 = -1, \mu_2 = 1$	$PD + CF + NS^{(2)}$	No
FNS	Fold-Neimark–Sacker	2	$\mu_{1,2} = e^{\pm i\theta}, \mu_3 = 1$	$NS + CF$	No
P	Codim-3 sing. cycles	3	$\mu_1 = -1, \mu_2 = 1$	$FF + GPD + R_{1:1}^{(2)} + CH^{(2)}$	Yes [(c)]
Q	Codim-3 sing. cycles	3	$\mu_{1,2} = -1, \mu_3 = 1$	$FF + R_{1:2} + FNS + CH + CH^{(2)}$	No

Table 3

Normal form coefficients corresponding to the Hopf–Hopf bifurcation (see (29)–(30) *in Appendix B) for the values of* η_3 *denoted by the dashed lines in Figure* 2(b).

η_3	$p_{11} \times p_{22}$	θ	δ	Θ	Δ	Case	Figure
0.7780	1	5.6245×10^{1}	-1.4914×10^{-1}	-5.6774×10^{5}	2.8800×10^{1}	S.III	3
0.7700	1	8.8924×10^{1}	-1.7423×10^{-1}	-1.8425×10^{6}	3.6525×10^{1}	S.III	5
0.7607	1	3.1039×10^{2}	-2.0475×10^{-1}	-6.2948×10^{7}	8.4121×10^{1}	S.III	9
0.7570	–1	-9.1810×10^{3}	-2.1733×10^{-1}	1.4948×10^{12}	-1.9094×10^{3}	D.VI	10

are depicted as solid curves when stable and dashed when unstable; blue is used for the cycle arising at H_1, orange for the cycle associated to H_2, and magenta for the cycle that undergoes the cyclic-fold bifurcation CF with the blue cycle. The actual size of the magenta cycle is considerably larger than the orange and blue cycles, and it was reduced in the figure to a scale compatible with the formers. The stable 2D torus is shown in black (see regions 7 and 8). Notice that in region 7 the 2D torus coexists with the equilibrium point and the three unstable cycles. The corresponding iterates at the Poincaré section (first and last rows) show the limit cycles as fixed points and the 2D torus as a closed curve with the same colors as those used in the phase planes.

The dynamics in the whole range of Figure 3 is illustrated in Appendix C by computing the largest Lyapunov exponent (see Figure 21). Notice that, for this value of η_3, neither the

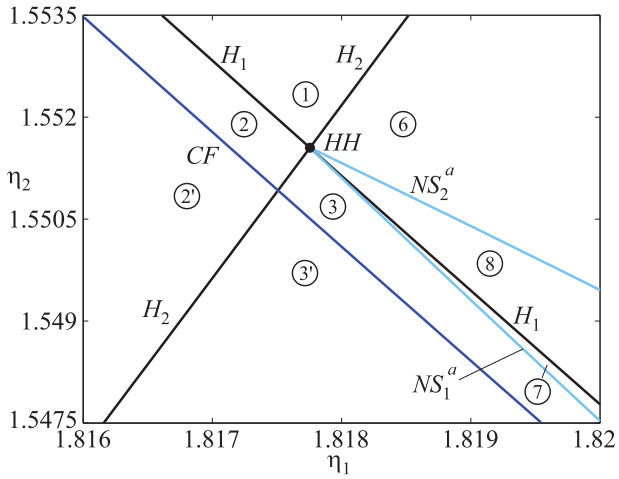

Figure 3. *Two-parameter bifurcation diagram for* $\eta_3 = 0.778$ *and* $\alpha_2 = 0.83$. *Normal form S.III.*

effect of the 2:3 resonance ($HH_{2:3}$) nor that of the degenerate curve (HH^0) is observed, and the dynamics is governed by the normal form of the Hopf–Hopf bifurcation.

3.2. Two-parameter slice at the left of $HH_{2:3}$ ($\eta_3 = 0.77$). When parameter η_3 is decreased to $\eta_3 = 0.77$, i.e., the point $HH_{2:3}$ is on the right of the corresponding vertical slice in Figure 2(b), a nontrivial bifurcation structure appears as shown in the semiglobal unfolding in Figure 5. The normal form of the Hopf–Hopf bifurcation does not change qualitatively and remains as the simple case S.III, with the coefficients shown in Table 3 (second row). As in the previous case, the (local) unfolding predicts only the existence of the Neimark–Sacker bifurcation curves NS_1^a and NS_2^a (see Figure 5(a)). In addition, a structure involving 1:2 and 1:3 strong resonances is detected. This nonlocal structure is shown in detail in the blow-ups of Figures 5(b) and 5(c). It is formed by a period-doubling (PD) bubble with two 1:2 strong resonance points ($R_{1:2}^{a,b}$) on the branch $NS_1^{a,b}$, and by a 1:3 strong resonance ($R_{1:3}$) on the branch $NS_2^{a,b}$. Both scenarios are connected by a curve of saddle-node bifurcations of limit cycles $CF^{(2)}$ arising at two generalized period-doubling bifurcation points $GPD^{a,b}$ on the PD bubble. In the following, the superscripts a and b included in the bifurcation acronyms will denote that the phenomenon is associated to the Neimark–Sacker branches NS_1^a or NS_1^b, respectively. The structure is completed with two secondary Neimark–Sacker bifurcation curves $NS^{(2)}$ beginning at $R_{1:2}^b$ (on the PD bubble) and at $R_{1:1}^{(2)}$ (near $R_{1:3}$), and ending at two 1:1 strong resonance points $R_{1:1}^{(2)}$ on $CF^{(2)}$. Two curves of neutral-saddle points (dashed lines) close the connection between the strong resonances $R_{1:2}^b$ and $R_{1:1}^{(2)}$. A similar structure for $\alpha_2 = 0.6$ was described in [25], where it was shown that it arises at $HH_{2:3}$.

The dynamics near the PD bubble is governed by period-two phenomena related to the cycle born at H_1, whereas the dynamics in the vicinity of $R_{1:3}$ is associated to period-three phenomena of the cycle arising at H_2. These phenomena will be described in detail next, but, to illustrate roughly the dynamics involved in this structure, two scenarios near the PD bubble and two near $R_{1:3}$ are included in Figure 6 by means of the phase planes and

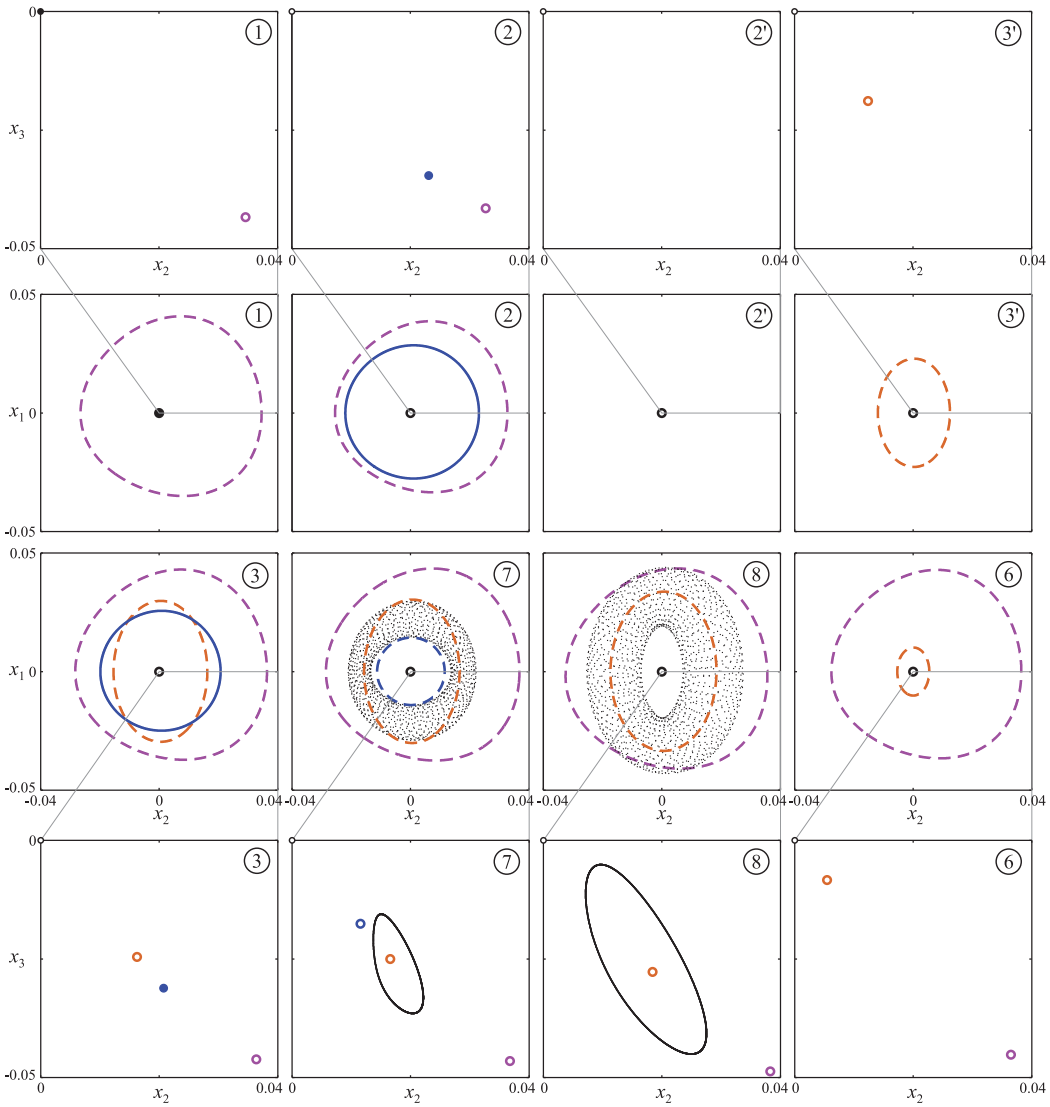

Figure 4. *Limit sets on the phase plane x_1-x_2 (second and third rows) and the associated Poincaré maps on the plane x_2-x_3 (first and fourth rows) for $x_1 = 0$ and $\dot{x}_1 > 0$.*

the corresponding Poincaré maps. The stable (unstable) limit cycles are denoted by solid (dashed) lines in the phase plane diagrams and by filled (empty) colored circles in the maps. Only stable tori are depicted in both diagrams (in black and gray). In Figure 6(a), the "period-one" limit cycle born at H_1 (in blue), the associated period-two cycles born at cyclic fold bifurcation $CF^{(2)}$ (in red and green), and the 2D torus (in black) arising when the blue cycle undergoes the Neimark–Sacker bifurcation NS_1, are appreciated. Figure 6(b) shows the scenario after the collapse of the blue cycle in H_1 and near the Neimark–Sacker bifurcation $NS^{(2)}$ of the "period-two cycle." The stable 2D torus (in gray) associated to the period-two cycle is observed. The period-two phenomena in Figures 6(a) and 6(b) evolve into period-

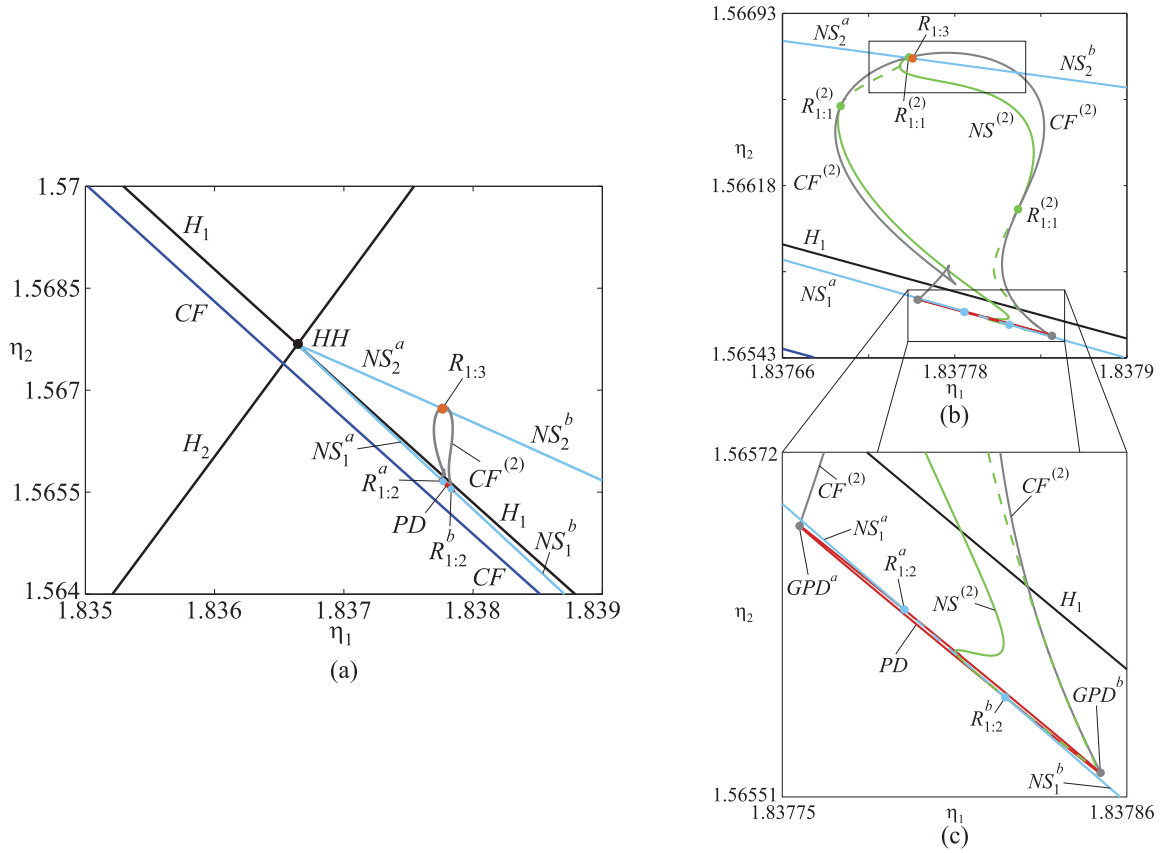

Figure 5. *Two-parameter bifurcation diagram for* $\eta_3 = 0.77$ *and* $\alpha_2 = 0.83$. *Normal form S.III.*

three phenomena, and analogous scenarios are observed near $R_{1:3}$ as depicted in Figures 6(c) and 6(d). The period-three cycles (in red and green) are also created by the $CF^{(2)}$ curve, but now they are associated to the cycle born at H_2 (in orange). The description of the global phenomena involved in the transition between both scenarios is beyond the scope of this paper; instead, our attention is focused on describing the structures around the PD bubble and the 1:3 strong resonance depicted by the rectangles in Figure 5(b).

The semiglobal scenarios around the PD bubble and the $R_{1:3}$ resonance coincide, respectively, with those observed in the analysis of k:2 and k:3 normal-internal resonances in quasi-periodically forced systems [4, 5, 27]. The dynamics in the vicinity of the PD bubble is illustrated in Figure 7 by means of selected Poincaré maps on the plane x_2-x_3 for $x_1 = 0$ and $\dot{x}_1 > 0$. A schematic representation of the blow-up of Figure 5(c) is also included in order to allow a better identification of the regions. The phase planes are not included, but the shapes of the orbits are similar to those shown in Figures 6(a) and 6(b). The limit sets are identified with the same colors used before (the orange limit cycle associated to H_2 is not included in Figure 7 since it has no direct participation in the dynamical phenomena of the PD bubble). The connection between the stable and unstable manifolds of the limit sets is depicted by means of the iterates at the Poincaré map. The period-one cycle (in blue) arises at H_1 and

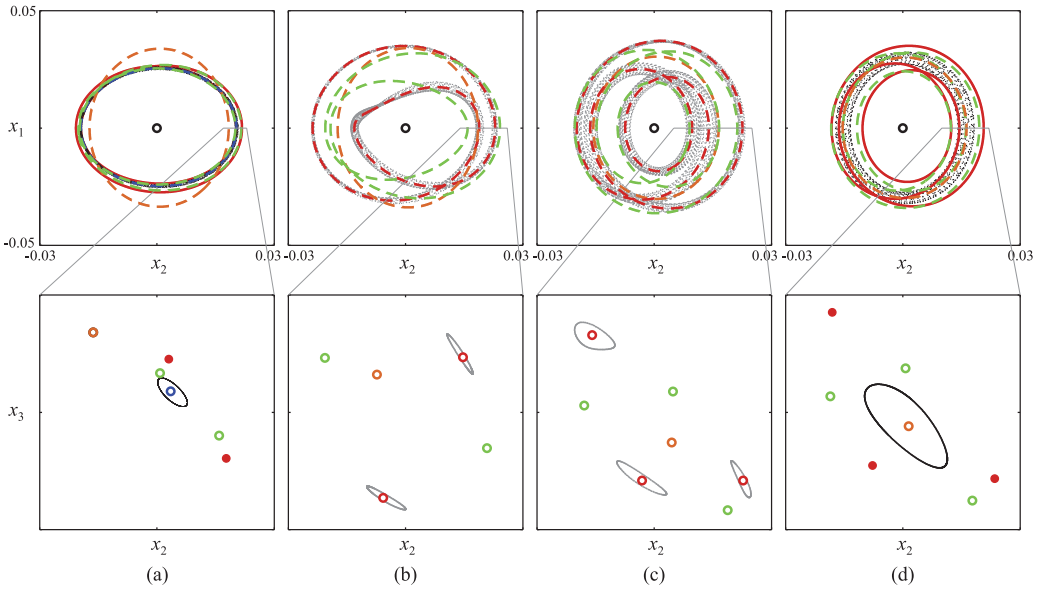

Figure 6. *Phase planes (first row) and the corresponding Poincaré maps (second row) for* $x_1 = 0$ *and* $\dot{x}_1 > 0$ *at different points near the PD bubble (*(a) *and* (b)*) and near* $R_{1:3}$ *(*(c) *and* (d)*).*

exists only in regions 1–8 and 12 (it does not exist in regions 9–11). The cycle undergoes period-doubling bifurcations on the PD bubble leading to the period-two cycles denoted in red and green (see, for example, the transitions from regions 12–1, 1–2, 8–7, or 7–6). The period-one cycle also undergoes Neimark–Sacker bifurcations on $NS_1^{a,b}$ leading to a 2D torus (closed curve in black) as occurs in the transitions 12–5, 2–3, and 12–8. The period-two cycles collapse on the cyclic-fold curves $CF^{(2)}$ (see transitions 3–5 and 6–8). The trajectory depicted in magenta represents the unstable manifold of the third period-one cycle (the "large" one in magenta (see Figure 4) not involved in the Hopf–Hopf bifurcation) that interacts with the blue cycle at the cyclic-fold bifurcation CF. Notice that global phenomena such as homoclinic and heteroclinic bifurcations and saddle-node bifurcations of tori, which explain the transitions between regions 3–4 and 9–10, are not included. The bifurcation diagram of this structure, including global phenomena, is described in [4, 5, 27] in relation to the normal form of the k:2 normal-internal resonances. In our case, the dynamics in the neighborhood of $R_{1:2}^b$ involves two Chenciner bifurcations CH and $CH^{(2)}$ enabling the transition from the dynamics given by the local unfolding of the 1:2 strong resonance to the dynamics shown in Figure 7. These phenomena introduce saddle-node bifurcations of tori, but they occur in an extremely narrow region of the parameter plane, and thus it is practically impossible to distinguish all of the regions in order to show the associated Poincaré maps.

The dynamics near $R_{1:3}$ is shown in Figure 8. The period-one limit cycle depicted in orange arises at the Hopf bifurcation branch H_2, and the period-three cycles in red and green are created (and collapsed) at the cyclic-fold bifurcation $CF^{(2)}$ (see transition 1–2). The orange cycle undergoes the Neimark–Sacker bifurcation $NS_2^{a,b}$ leading to a stable 2D torus (denoted by the black closed curve in maps 1 and 4). This torus exhibits heteroclinic connections with

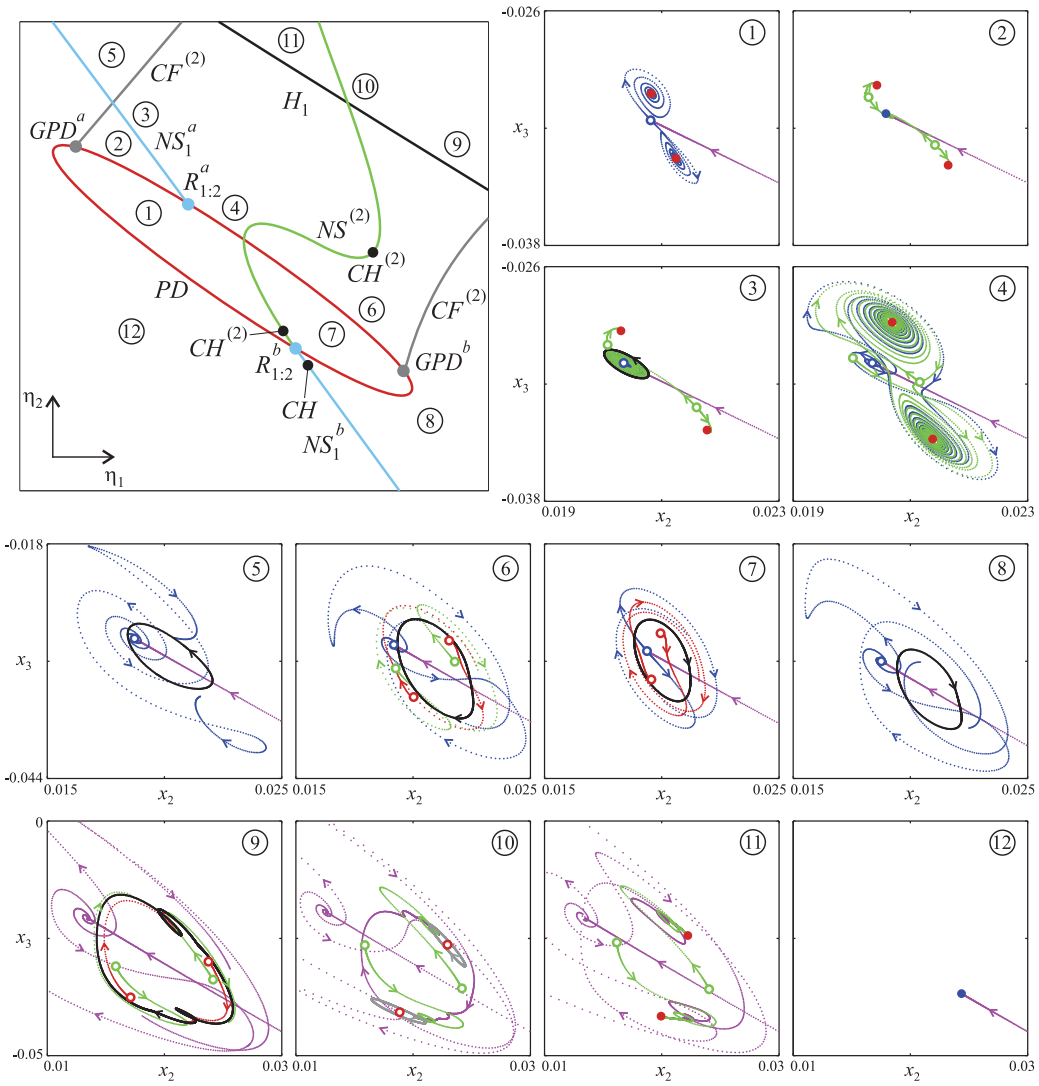

Figure 7. *Blow-up of the bifurcation diagram of Figure 5(c) in the neighborhood of $R^{a,b}_{1:2}$, and projections of the relevant Poincaré maps for $x_1 = 0$ and $\dot{x}_1 > 0$.*

the green period-three cycle (predicted by the normal form of the Neimark–Sacker bifurcation), enabling the transitions between regions 2–3 and 3–4 (and also 5–6 and 6–7). A secondary stable torus (gray cycle in regions 5, 6, and 7) is created by a Neimark–Sacker bifurcation of the red period-three cycle on the curve $NS^{(2)}$ originating at $R^{(2)}_{1:1}$ (see transitions 2–7, 3–6, and 4–5). The Chenciner bifurcation $CH^{(2)}$ on $NS^{(2)}$ indicates the presence of a curve of saddle-node of tori associated to the gray torus. We do not show the heteroclinic curves associated to the black torus and the saddle-node of the gray torus since they were not computed. The diagram (excluding the cyclic-fold bifurcation $CF^{(2)}$ and $NS^{(2)}$) is described in [5] in relation to the analysis of k:3 normal-internal resonance.

To expose the complexity introduced by the whole structure, the largest Lyapunov

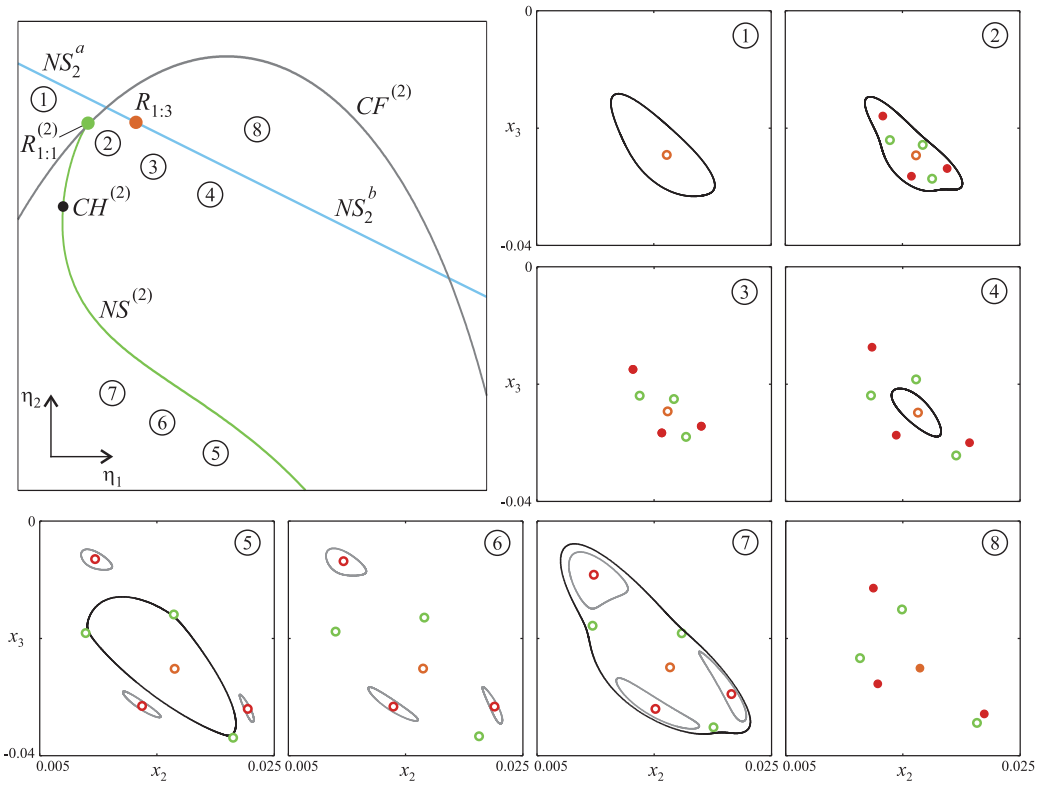

Figure 8. *Blow-up of the bifurcation diagram of Figure* 5(b) *in the neighborhood of* $R_{1:3}$*, and projections of the relevant Poincaré maps for* $x_1 = 0$ *and* $\dot{x}_1 > 0$.

exponent diagram on the parameter plane $\eta_1 - \eta_2$ is computed in Figure 22 in Appendix C. The main difference between this case ($\eta_3 = 0.77$) and the previous one ($\eta_3 = 0.778$) is the dynamics around the ensemble of resonant bifurcations (see Figure 22(b)).

3.3. Two-parameter slice at the right of HH^0 ($\eta_3 = 0.7607$). For decreasing values of parameter η_3, the cyclic-fold bifurcation curve CF (observed previously in the diagrams of Figures 3 and 5) interacts with the period-doubling bubble PD, paving the way for the birth of additional phenomena. This is revealed in Figure 9(a) and in the corresponding blow-ups of Figures 9(b) and 9(c) for $\eta_3 = 0.7607$. Notice that the deepest blow-up of Figure 9(c) is a schematic representation since it is very difficult to distinguish the curves in the actual bifurcation diagram. The local unfolding of the Hopf–Hopf bifurcation remains without qualitative changes, i.e., it is the case S.III (see the coefficients in Table 3). As shown in Figure 9(c), the interaction between CF with the PD bubble and GPD introduces new phenomena: two fold-flip bifurcation points $FF^{a,b}$ and a 1:1 strong resonance of a period-two cycle $R_{1:1}^{(2)a}$, which change the connections of the $NS^{(2)}$ curve and generate a twist in the PD bubble. The higher codimension bifurcation leading to these phenomena, and the new features introduced in the dynamics, is associated to the interaction between HH^0 and $HH_{2:3}$, and it will be analyzed in detail in the next section.

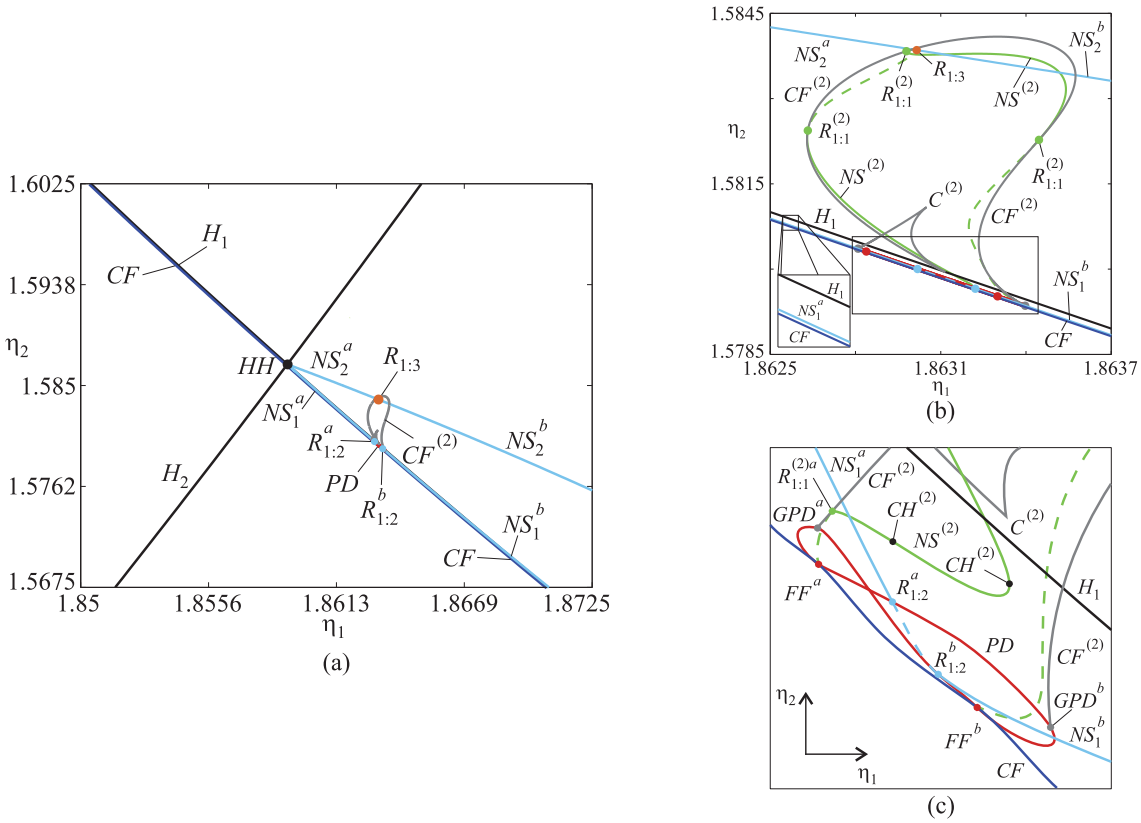

Figure 9. *Two-parameter bifurcation diagram for* $\eta_3 = 0.7607$ *and* $\alpha_2 = 0.83$. *Normal form S.III.*

3.4. Two-parameter slice at the left of HH^0 ($\eta_3 = 0.757$). Both fold-flip bifurcations disappear for lower values of η_3, as is depicted for $\eta_3 = 0.757$ in Figure 10(a) and in the blow-ups of Figures 10(b) and 10(c). Again the deepest blow-up (Figure 10(c)) is a schematic representation of the actual bifurcation diagram. The fold-flip interaction has disappeared and the cyclic-fold curve CF now interacts with H_1 by means of two generalized Hopf bifurcations (GH in Figure 10(a)). In addition, the twist in the PD bubble disappeared and a new 1:1 strong resonance of the period-two cycle $R_{1:1}^{(2)b}$ was created. In this case, as a consequence of the degenerate Hopf–Hopf bifurcation HH^0, the local unfolding of the Hopf–Hopf bifurcation has changed to the difficult case D.VI, with the coefficients given in the last row of Table 3.

This two-parameter analysis reveals a bifurcation structure associated to the 2:3 resonant Hopf–Hopf bifurcation, and additional codimension-two bifurcation points, namely, fold-flip bifurcations, generalized Hopf bifurcations, and Neimark–Sacker 1:1 strong resonances, exposing the effect of the degenerate condition HH^0 that will be analyzed in the next section.

4. Numerical three-parameter semiglobal unfolding of the 2:3 resonant Hopf–Hopf bifurcation near the degenerate condition. In order to identify the mechanism leading to the interactions between the cyclic-fold curve CF with the limit-cycle bifurcations PD, $GPD^{a,b}$, $R_{1:2}^{a,b}$, and $NS_1^{a,b}$ exposed in Figures 9 and 10, the relevant codimension-two bifurcation points

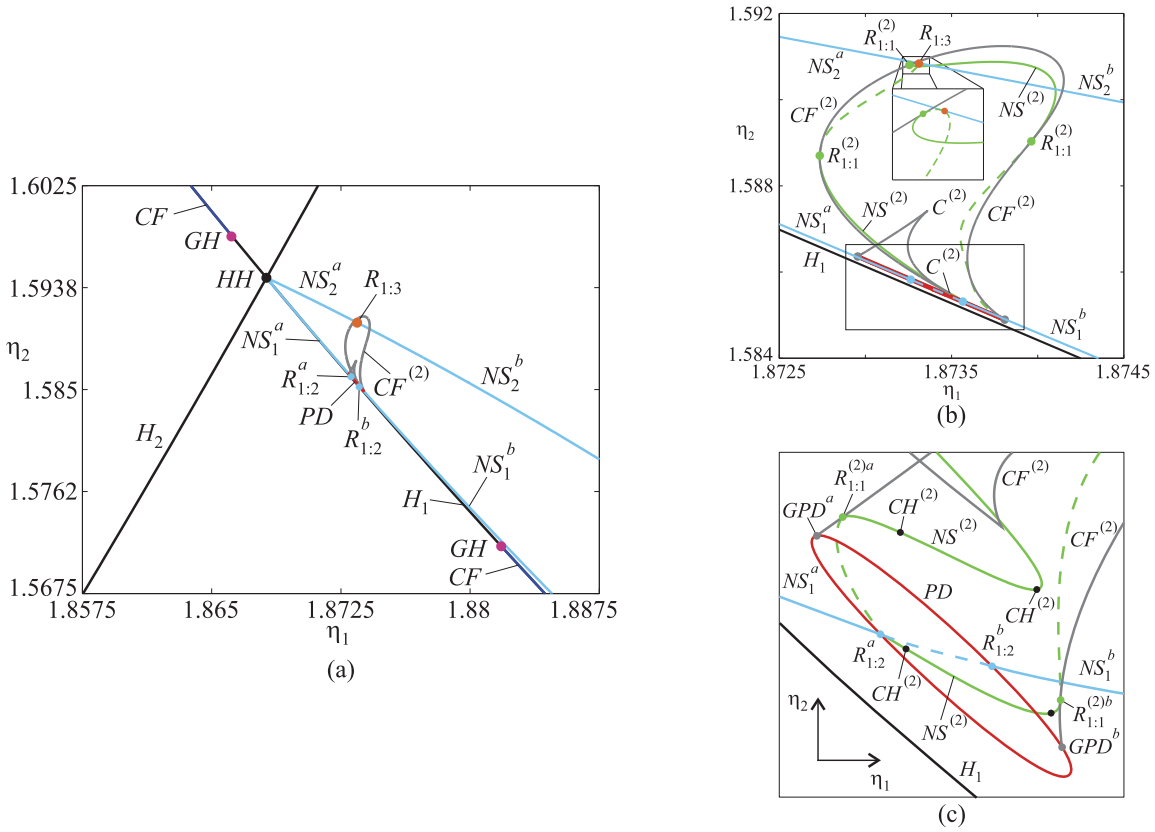

Figure 10. *Two-parameter bifurcation diagram for* $\eta_3 = 0.757$ *and* $\alpha_2 = 0.83$. *Normal form D.VI.*

detected before for $\alpha_2 = 0.83$ are continued in the main parameter space (η_1, η_2, η_3). The continuation results, completing those shown in Figure 2, are depicted in Figures 11(a) and 11(b), with the corresponding blow-ups in Figures 12(a)–12(d). Figures 11(a) and 11(b) show that the 1:2 and 1:3 strong resonance curves $R^{a,b}_{1:2}$ and $R_{1:3}$, and a pair of generalized period-doubling bifurcations $GPD^{a,b}$, arise at $HH_{2:3}$. Therefore, as shown in [25] for $\alpha_2 = 0.6$, the 2:3 resonant Hopf–Hopf singularity acts as an organizing center of the dynamics in the main parameter space. The three-parameter bifurcation diagram includes the 1:1 resonant Hopf–Hopf point $HH_{1:1}$ that unfolds a fold-Neimark–Sacker curve (FNS) and a generalized Hopf curve (GH) corresponding to the vanishing of the first Lyapunov coefficient of the branch H_1. The curve GH interacts with the Hopf–Hopf bifurcation HH at the codimension-three bifurcation point HH^0, where the nondegeneracy condition of the Hopf–Hopf normal form fails, and the fold-Neimark–Sacker curve FNS^a arises (see Figures 12(a) and 12(b)).

Other codimension-two and -three phenomena denoted in these diagrams are not explained by the 2:3 resonant Hopf–Hopf singularity or by HH^0 or $HH_{1:1}$. These phenomena are organized around a fold-flip bubble FF and four codimension-three bifurcation points $P^{a,b}$ and $Q^{a,b}$ (see Figures 12(c) and 12(d)). A brief introduction of this structure is given here and a detailed description is included in section 5. At the singular points $P^{a,b}$ the fold-flip bubble interacts with the curves $GPD^{a,b}$, respectively. As a result, one of the coefficients of

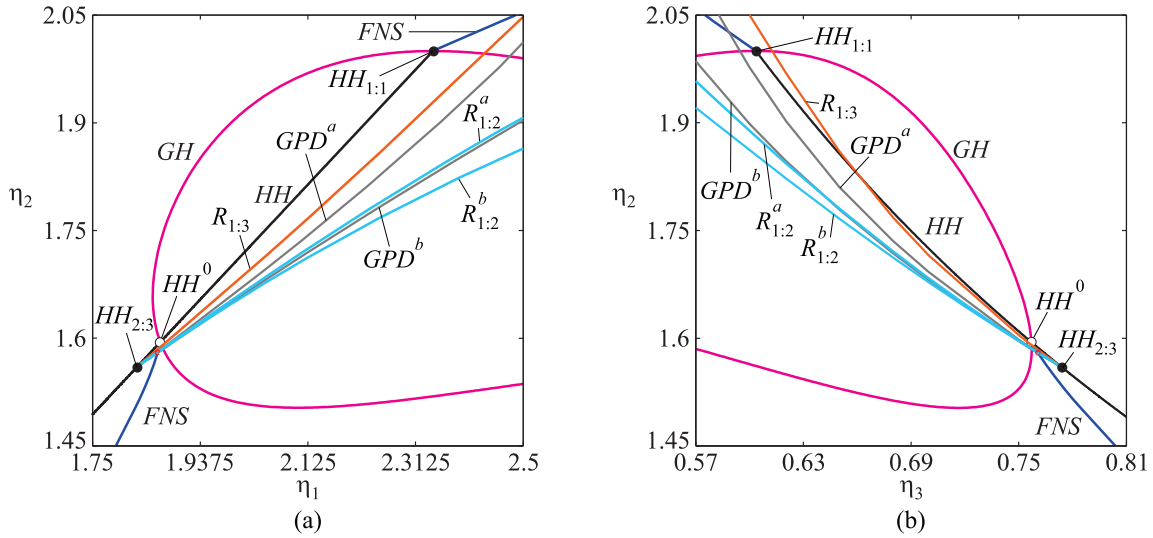

Figure 11. *Three-parameter bifurcation diagrams for* $\alpha_2 = 0.83$.

the fold-flip normal form vanishes, and a curve of 1:1 strong resonances of a period-two cycle, denoted as $R_{1:1}^{(2)a,b}$, arises. The singularity P^b also introduces a Chenciner $CH^{(2)}$ bifurcation curve of a period-two torus. On the other hand, $Q^{a,b}$ relates the fold-flip bifurcation FF to the 1:2 strong resonance curves $R_{1:2}^{a,b}$ and the fold-Neimark–Sacker curves $FNS^{a,b}$. Notice that FNS^a connects Q^a with HH^0. In addition, $Q^{a,b}$ unfolds Chenciner curves, denoted CH and $CH^{(2)}$ in Figures 12(c) and 12(d). The nontrivial Floquet multipliers at $Q^{a,b}$ are $(-1, -1, 1)$.

Different methods were used for computing codimension-two bifurcation curves. The generalized Hopf bifurcation curve GH was obtained by using the frequency domain method [22, 23]. Thus, the first Lyapunov coefficient was computed, and the conditions on the parameters leading to the vanishing of this coefficient were obtained. The FF curve was computed with LOCBIF [14], starting at the points detected in the two-parameter bifurcation diagrams. The remaining curves were obtained with Matcont by performing 2D slices in the parameter plane $\eta_1 - \eta_2$ for different values of η_3 and then connecting the points. This "artisanal" method was also used for computing the codimension-three bifurcation curves appearing below.

5. Analysis of the fold-flip bubble and its singular points $P^{a,b}$ and $Q^{a,b}$. Let us consider 2D bifurcation diagrams in the parameter plane $\eta_1 - \eta_2$ for some key values of η_3. These slices of the three-parameter bifurcation diagram are denoted by the vertical dashed lines with labels a–f in Figure 12(d), and the results are represented schematically in Figure 13(a)–(f), respectively. The locations of the interacting bifurcations and their normal form coefficients are given in Tables 4 and 5, respectively. Let us begin with a description of the interactions from the right to the left in Figure 12(d), i.e., for decreasing values of η_3.

5.1. Effects of the FF bubble and FNS on the bifurcation structure. The scenario at the right of the fold-flip bubble FF is similar to the one observed in Figure 5 for $\eta_3 = 0.77$. For $\eta_3 = 0.7608$, i.e., on the slice a in Figure 12(d), the PD bubble retains both 1:2 strong

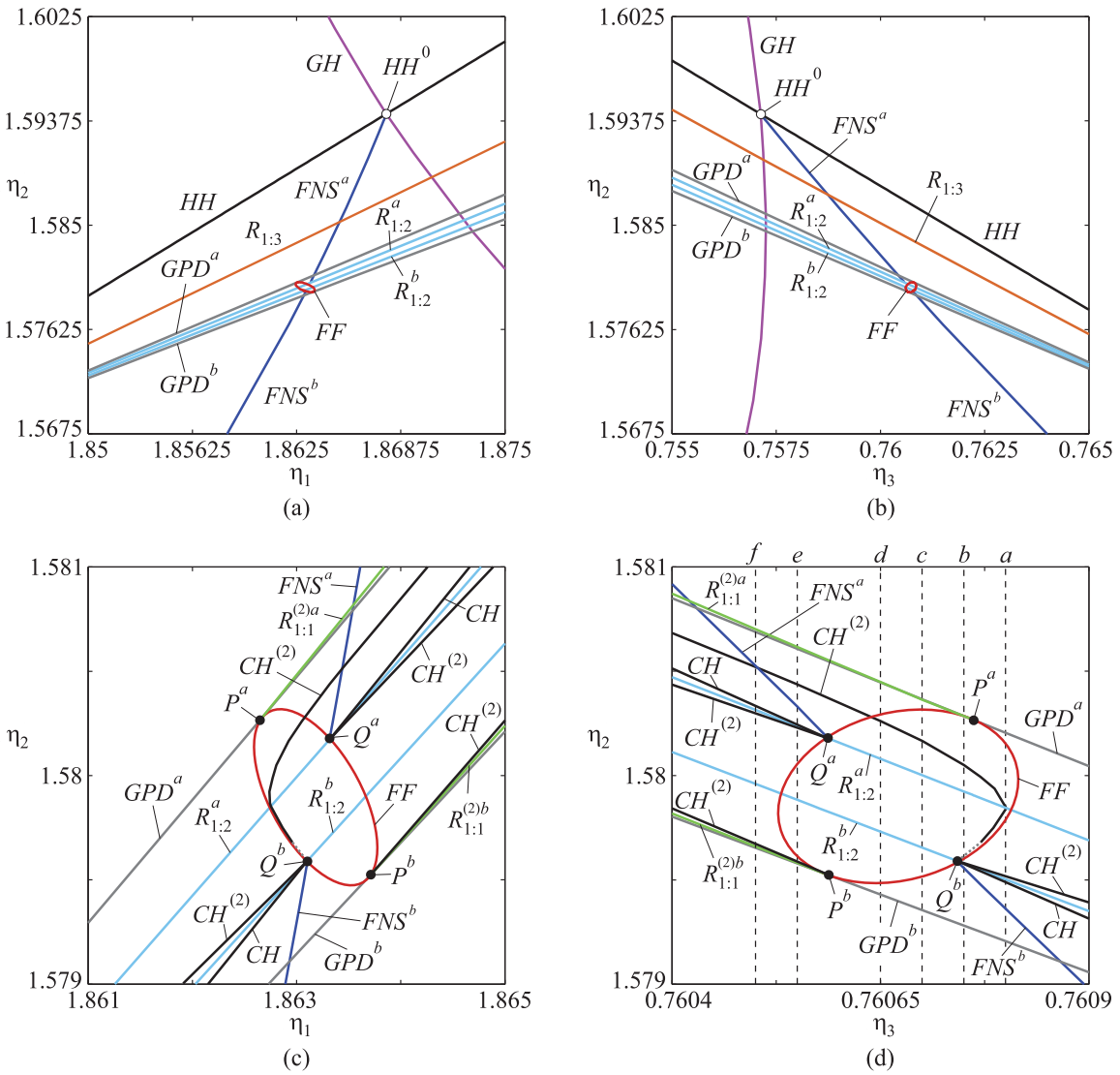

Figure 12. *Blow-ups corresponding to the three-parameter bifurcation diagrams of Figure 11 for* $\alpha_2 = 0.83$.

resonances $R^{a,b}_{1:2}$ and both generalized period-doubling bifurcations $GPD^{a,b}$ as show in Figure 13(a). According to the coefficients of the normal form (see Table 5), the unfoldings of $R^a_{1:2}$ and $R^b_{1:2}$ correspond to the ones shown in Figures 9.9 and 9.10 of [18], respectively. Both scenarios coincide with those in our Figure 13(a) (global bifurcations are not included). Notice that only the 1:2 resonance $R^b_{1:2}$ unfolds a supercritical Neimark–Sacker curve $NS^{(2)}$ since $a < 0$ and $b > 0$. The scenario is completed with two Chenciner bifurcations on the Neimark–Sacker curves NS^b_1 and $NS^{(2)}$, denoted as CH and $CH^{(2)}$, respectively. On the other hand, the normal form coefficient e of the generalized period-doubling bifurcation GPD^a is negative and the unfolding corresponds to the one shown in Figure 9.3 of [18]. The coefficient of GPD^b is positive and the unfolding is the opposite of the one of GPD^a.

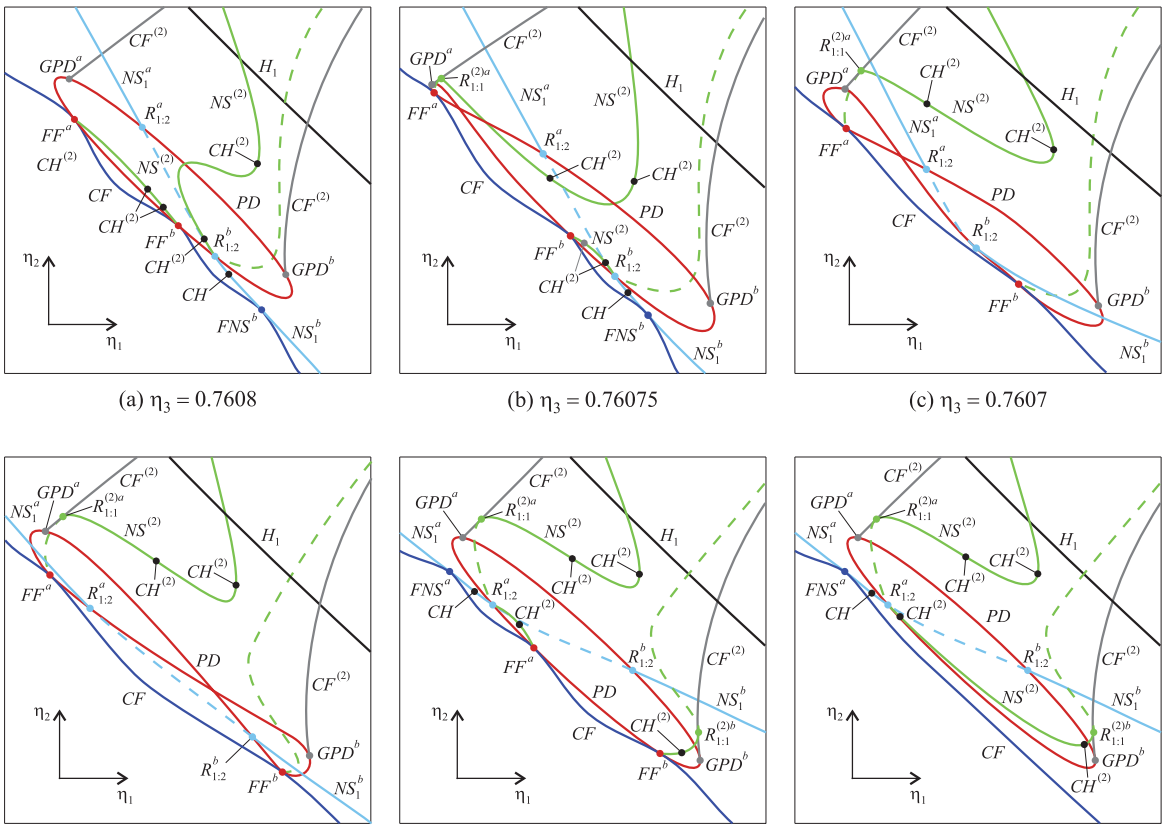

Figure 13. *Two-parameter bifurcation diagrams (schematics) across the fold-flip bubble for* $\alpha_2 = 0.83$.

The first influence of the fold-flip bubble on the bifurcation diagram is introduced by the two fold-flip points $FF^{a,b}$. The normal form coefficients of $FF^{a,b}$ are also included in Table 5. According to [6], since in both cases $a_{02} \times b_{11} < 0$ and $C_{NS} < 0$, each fold-flip point unfolds a supercritical Neimark–Sacker curve ($NS^{(2)}$) of the period-two cycle. In this case, $NS^{(2)}$ is a single curve joining FF^a and FF^b (as depicted in Figure 13(a)) with two Chenciner bifurcations $CH^{(2)}$. A second addition to the bifurcation structure is the fold-Neimark–Sacker bifurcation point FNS^b. The normal form coefficients, computed according to the procedure described in [7, 8], reveal that the unfolding corresponds to the one shown in Figure A1(c) of [8] for $s = 1$, $\theta < 0$, and $E > 0$ and contemplates the existence of an unstable 3D torus. This torus is destroyed via a complicated global phenomena (homoclinic tangle) occurring in an exponentially small wedge in the parameter space (see [18, 32, 8]).

The dynamics related to the bifurcation scenario in Figure 13(a) is illustrated in Figure 14. The phase portraits on regions 1–12 coincide with those in Figure 7, and the ones related to the bifurcations $FF^{a,b}$ and FNS^b are depicted by means of schematic local unfoldings and their associated Poincaré maps. The new scenario is governed by the interaction between the the cycle originated by the cyclic-fold curve CF and the limit sets associated to the PD bubble.

Table 4

Bifurcation points with superscripts a and b in the diagrams shown in Figures 13(a)–13(f).

	η_3	FF^a		$R^a_{1:2}$		GPD^a		FNS^a	
		η_1	η_2	η_1	η_2	η_1	η_2	η_1	η_2
(a)	0.76080	1.862743	1.579845	1.862584	1.580118	1.862536	1.580198	-	-
(b)	0.76075	1.862881	1.579923	1.862673	1.580278	1.862673	1.580279	-	-
(c)	0.76070	1.863018	1.580001	1.862838	1.580311	1.862809	1.580359	-	-
(d)	0.76065	1.863156	1.580080	1.863038	1.580282	1.862946	1.580440	-	-
(e)	0.76055	1.863568	1.580003	1.863431	1.580236	1.863218	1.580601	1.863375	1.580332
(f)	0.76050	-	-	1.863569	1.580315	1.863355	1.580681	1.863445	1.580527
	η_3	FF^b		$R^b_{1:2}$		GPD^b		FNS^b	
		η_1	η_2	η_1	η_2	η_1	η_2	η_1	η_2
(a)	0.76080	1.862745	1.579841	1.862944	1.579502	1.863118	1.579206	1.863026	1.579362
(b)	0.76075	1.863060	1.579617	1.863083	1.579578	1.863258	1.579281	1.863096	1.579556
(c)	0.76070	1.863300	1.579521	1.863222	1.579655	1.863397	1.579355	-	-
(d)	0.76065	1.863505	1.579485	1.863360	1.579731	1.863537	1.579430	-	-
(e)	0.76055	1.863568	1.580003	1.863638	1.579884	1.863817	1.579579	-	-
(f)	0.76050	-	-	1.863777	1.579960	1.863957	1.579653	-	-

Table 5

Normal form coefficients of the bifurcation points with superscripts a and b of Figures 13(a)–13(f). The values in brackets (e.g., $[10^{-3}]$) indicate a scale factor of the corresponding coefficient.

	η_3	FF^a				$R^a_{1:2}$		GPD^a	FNS^a		
		a_{20} $[10^{-3}]$	a_{02} $[10^{-4}]$	b_{11}	C_{NS}	a $[10^{-1}]$	b $[10^5]$	e $[10^9]$	s	θ	E
(a)	0.76080	4.1178	1.3644	-1.8507	-8.9634	2.9203	-4.2929	-5.8797	-	-	-
(b)	0.76075	4.0583	1.8156	0.1390	-	3.8690	-7.4499	-100.43	-	-	-
(c)	0.76070	3.9975	1.9739	1.9798	-	5.6924	-15.942	-4.1026	-	-	-
(d)	0.76065	3.9363	1.9933	5.5875	-	10.607	-54.798	-1.1052	-	-	-
(e)	0.76055	3.8121	1.5230	-7.8798	-566.38	-15.294	-111.30	-0.2852	1	-320	-4516
(f)	0.76050	-	-	-	-	-6.9714	-22.869	-0.1844	1	-325	-1014
	η_3	FF^b				$R^b_{1:2}$		GPD^b	FNS^b		
		a_{20} $[10^{-3}]$	a_{02} $[10^{-4}]$	b_{11}	C_{NS}	a $[10^{-1}]$	b $[10^5]$	e $[10^7]$	s	θ	E
(a)	0.76080	4.1151	0.7337	-5.1269	-85.111	-1.3484	6.4661	1.3518	1	-297	2204
(b)	0.76075	4.0521	0.3053	-39.489	-5951.8	-8.3582	247.77	2.3048	1	-301	8374
(c)	0.76070	3.9906	0.1677	8.4332	-	1.9996	14.145	4.8444	-	-	-
(d)	0.76065	3.9296	0.1670	2.5796	-	0.8947	2.8244	16.152	-	-	-
(e)	0.76055	3.8094	0.6684	-1.6483	-2.9738	0.4262	0.6376	34.083	-	-	-
(f)	0.76050	-	-	-	-	0.3381	0.4003	0.7419	-	-	-

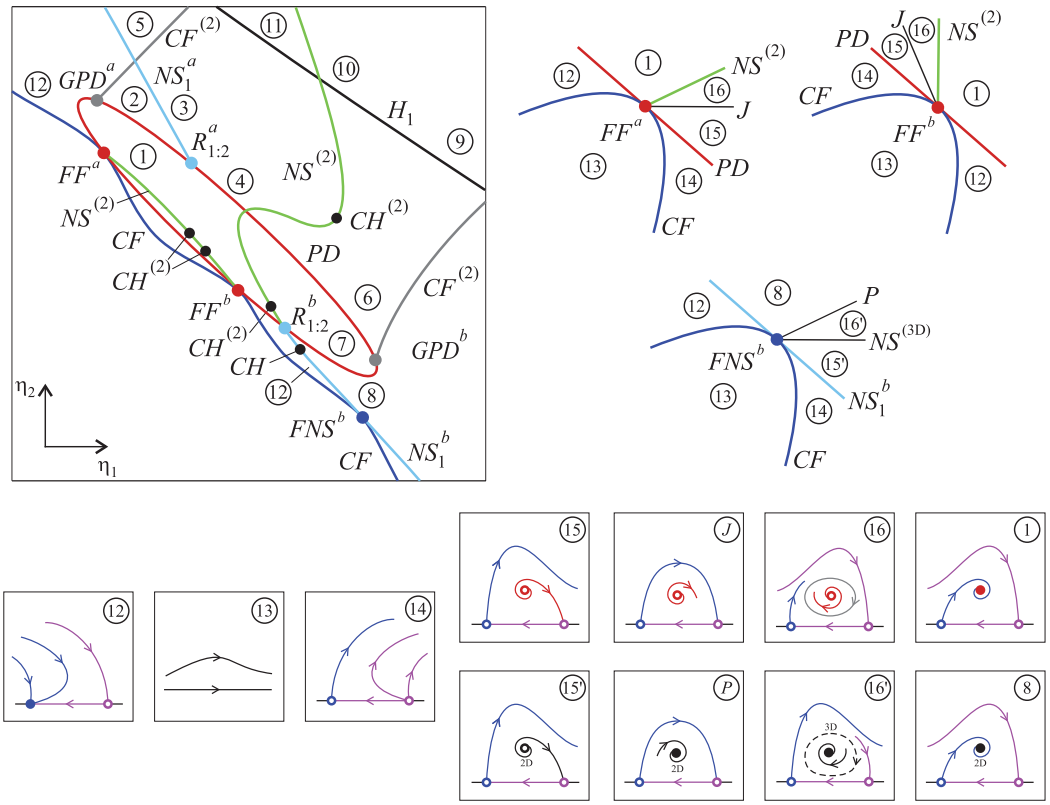

Figure 14. *Two-parameter bifurcation diagram and Poincaré maps for* $\eta_3 = 0.7608$ *(Figure* 13(a)*).*

Thus, the period-one cycle in magenta is introduced to the ensemble, interacting not only with the cycle born at H_1 (in blue) but also with the period-two phenomena related to the PD bubble, namely, the period-two cycle (red dot in regions 15, 16, and 1) and the 2D torus (gray closed curve in region 16). In addition, the fold-Neimark–Sacker bifurcation FNS^b introduces another 2D torus (see the black dot in regions 15′, 16′, and 8) and an unstable 3D torus (closed dashed curve in region 16′). Notice that the dot above the horizontal axis represents a period-two cycle in the unfoldings of the fold-flip, and a 2D torus in the unfolding of the fold-Neimark–Sacker bifurcation. On the other hand, the closed curve is a 2D torus in the fold-flip diagrams and a 3D torus in the fold-Neimark–Sacker. In order to illustrate the actual dynamics associated to the FNS^b phenomenon, a simulation of the limit sets and transient behavior in region 8, very close to the heteroclinic curve P, is shown in Figure 15. In this figure the period-one cycles are unstable and the only stable set is the 2D torus (see the Poincaré map corresponding to region 8 in Figure 14). A slow transient behavior, reminiscent of the heteroclinic orbit (cf. Figure 8.20 in [18]) and associated to the connection of the manifolds of the cycles, appears.

5.2. Effects of singularity P^a on the bifurcation structure. Decreasing η_3 from $\eta_3 = 0.7608$ (Figure 13(a)) to $\eta_3 = 0.76075$ (Figure 13(b)), the GPD^a curve interacts with the FF bubble in a codimension-three bifurcation labeled P^a in Figure 12(d). At this point, GPD^a

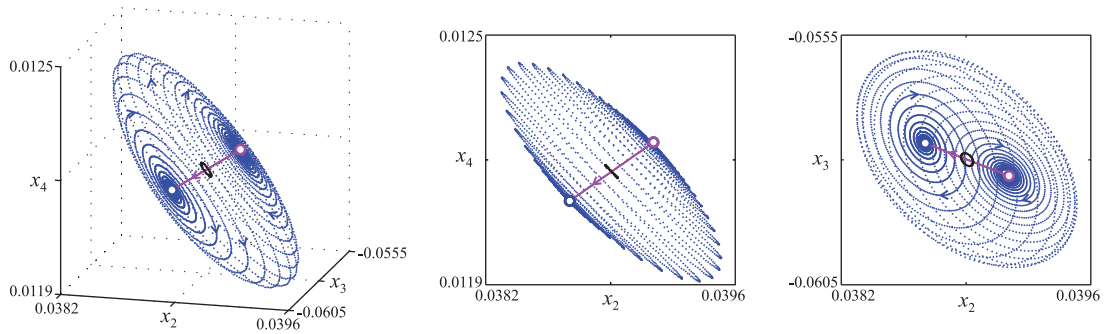

Figure 15. *Dynamical behavior in region 8 near the P curve for $\eta_3 = 0.7608$. The transient behavior resembles the heteroclinic orbit associated to the connection of the manifolds of the cycles.*

becomes singular ($e \to -\infty$) and, simultaneously, a degeneration is introduced on the fold-flip bifurcation, which is denoted by the vanishing of the normal form coefficient b_{11}. After P^a, the normal form of GPD does not change but FF^a changes, as denoted in Table 5 for $\eta_3 = 0.76075$. Since $a_{02} \times b_{11} > 0$, now FF^a does not unfold the $NS^{(2)}$ bifurcation, as depicted in the schematic diagram of the numerical continuation shown in Figure 13(b). The interaction between FF^a and GPD^a at P^a introduces a 1:1 strong resonance $R^{(2)a}_{1:1}$ on the cyclic-fold branch $CF^{(2)}$ (originated at GPD^a). Then, the Neimark–Sacker curve $NS^{(2)}$, originally associated to FF^a, is transferred to $R^{(2)a}_{1:1}$. In this case, the curve is supercritical (as before) since the product of the normal form coefficients of $R^{(2)a}_{1:1}$ (not included in Tables 4 and 5) is negative ($a \times b < 0$) [18, 6]. This product remains negative throughout the curve $R^{(2)a}_{1:1}$ in Figures 12(c) and 12(d), and the unfolding is equivalent to the one shown in Figure 8.8 of [18]. The interaction between FF^a and GPD^a (and the one between FF^b and GPD^b explained below) can be interpreted within the framework of quasi-periodic Hopf bifurcations discussed in [30]. In particular, the slices shown in Figures 13(a),(b) can be associated to the connections at the right in Figures 4 and 2 of [30], respectively. The latter presents different unfoldings of the FF and $R^{(2)}_{1:1}$ bifurcations (associated to the singularities SH and BT, respectively, in [30]).

Notice that in the slice shown in Figure 13(b) the bifurcations FF^b and $R^b_{1:2}$ share the same Neimark–Sacker curve $NS^{(2)}$. This is due to a global interaction between the Neimark–Sacker curve joining FF^a with FF^b and the Neimark–Sacker curve originating at $R^b_{1:2}$ (both shown in Figure 13(a)). This global phenomenon occurs between $\eta_3 = 0.7608$ and $\eta_3 = 0.76075$ (Figures 13(a),(b), respectively), when both curves collide and split, leaving FF^b and $R^b_{1:2}$ connected by the same Neimark–Sacker curve and FF^a with the curve formerly associated to $R^b_{1:2}$. Chenciner bifurcations CH and $CH^{(2)}$ complete the scenario. It is worth noting that the point $CH^{(2)}$ in gray, near FF^b, could not be detected numerically but it must exist in order to make consistent the normal forms of FF^b and $R^b_{1:2}$. The existence is also conjectured by noticing the bifurcation diagram in Figures 12(c) and 12(d), where a curve of $CH^{(2)}$ points was traced to the vicinity of Q^b (the actual continuation is denoted as a solid black curve and the conjectured one as the dashed gray segment).

Finally, after P^a, the PD bubble is twisted at the top, leading to an "eight" figure. The

twist will be rectified later at the interaction of FF^b with GPD^b (point P^b in Figure 12(d)). A bubble with a similar twisting was observed in [2] but considering Neimark–Sacker bifurcation (Hopf of periodic orbits) and neutral-saddle curves instead of period-doubling bifurcation.

5.3. Effects of singularity Q^b on the bifurcation structure. For lower values of η_3, a second codimension-three bifurcation occurs at the point labeled Q^b in Figure 12(d). In this case, the interaction is between the curves FF^b, $R^b_{1:2}$, FNS^b, CH, and $CH^{(2)}$, and the nontrivial Floquet multipliers of the involved limit cycle are $\mu_{1,2} = -1$ and $\mu_3 = 1$. As was shown in [28] and [11], bifurcations of periodic orbits like this can lead to complex dynamics, more precisely, Lorenz-like attractors. The curve FNS^b ends at this singularity, and thus the two-parameter bifurcation diagram for decreasing values of η_3, i.e., on the left of Q^b, does not contain the bifurcation point FNS^b. In addition, Q^b changes the normal forms of FF^b and $R^b_{1,2}$. The effect of Q^b is exhibited when comparing the scenarios in Figure 13(b) for $\eta_3 = 0.76075$ (slice b on the right of Q^b) with the one in Figure 13(c) for $\eta_3 = 0.7607$ (slice c on the left of Q^b), and the corresponding normal form coefficients in Table 5. In this case, neither FF^b nor $R^b_{1:2}$ unfolds Neimark–Sacker curves, since $a_{02} \times b_{11} > 0$ for FF^b and $a > 0$ for $R^b_{1:2}$.

Figure 13(d) shows the situation for $\eta_3 = 0.76065$ (slice d). It does not differ qualitatively from the one in Figure 13(c) for $\eta_3 = 0.7607$, but in this projection, the strong resonance point $R^a_{1:2}$ appears on the lower part of the PD bubble due to the twist of the curve.

Notice that for values of η_3 between P^a and Q^a neither the bifurcation points FF^a nor $R^a_{1:2}$ unfold $NS^{(2)}$ curves. The same is valid for FF^b and $R^b_{1:2}$ between the points Q^b and P^b. Moreover, fold-Neimark–Sacker bifurcations do not exist between Q^a and Q^b.

5.4. Effects of singularities Q^a and P^b on the bifurcation structure. The transition between Figures 13(d) and 13(e) (i.e., slices d and e in Figure 12(d), respectively) denotes the effects of the singularities Q^a and P^b, simultaneously. Decreasing the parameter from $\eta_3 = 0.76065$ (slice d) to $\eta_3 = 0.76055$ (slice e), the resonance $R^a_{1:2}$ interacts with FF^a in another codimension-three bifurcation with multipliers $\mu_{1,2} = -1$ and $\mu_3 = 1$. This point is labeled as Q^a in Figure 12(d). As a consequence, $R^a_{1:2}$ and FF^a change their unfoldings, introducing a secondary torus by means of the $NS^{(2)}$ curve that connects both bifurcation points (see Figure 13(e)). Nevertheless, the Neimark–Sacker curve unfolded by $R^a_{1:2}$ is subcritical (since $a < 0$ and $b < 0$ in Table 5), while the one generated by FF^a is supercritical ($C_{NS} < 0$ in Table 5). The connection of these branches is possible due to a Chenciner bifurcation (labeled $CH^{(2)}$ in Figure 13(e)). In addition, a fold-Neimark–Sacker bifurcation (FNS^a) appears on NS^a_1, when Q^a is crossed. The unfolding of the normal form of FNS^a is the same as FNS^b but with a time reversion, since $E < 0$. Hence the stability of all limit sets are interchanged and the 3D torus is stable. The Poincaré map of the stable 3D torus and the unstable period-one cycles near FNS^a is depicted in Figure 16.

Almost immediately after Q^a, the fold-flip bubble FF interacts with GPD^b at the point P^b (in a way similar to FF^a and GPD^a). This interaction changes the unfolding of FF^b, generating a period-two Neimark–Sacker curve. Another 1:1 strong resonance is also created (namely, $R^{(2)b}_{1:1}$ in Figure 13(e)) and shares the same $NS^{(2)}$ curve with FF^b. In this case, the Neimark–Sacker curve originating at FF^b is supercritical ($C_{NS} < 0$ in Table 5), while the one associated to $R^{(2)b}_{1:1}$ is subcritical (since the product of the normal form coefficients is

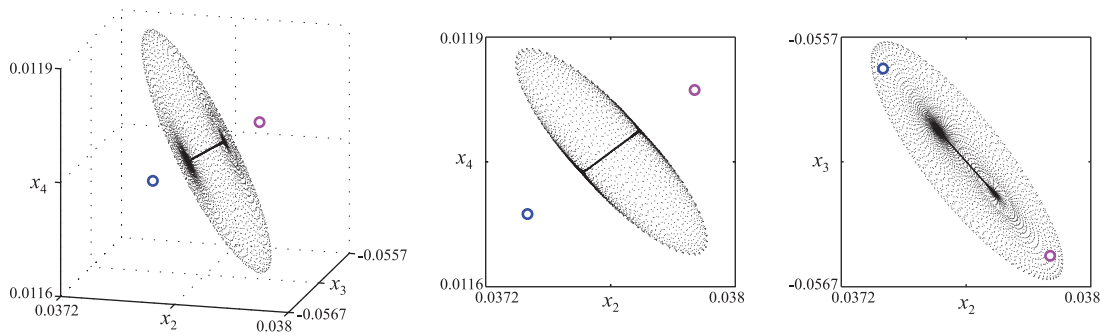

Figure 16. *Poincaré map corresponding to the stable 3D torus observed near FNS^a for $\eta_3 = 0.76055$.*

positive, $a \times b > 0$). Again, the connection is possible via a Chenciner bifurcation, namely, $CH^{(2)}$ in Figure 13(e). The Chenciner bifurcations encountered throughout the diagrams in Figure 13 (and the corresponding curves shown in Figures 12(c) and 12(d)) were detected during the continuation of the Neimark–Sacker curves. These singularities serve as a connecting mechanism between the fold-flip and $R_{1:2}$ and $R^{(2)}_{1:1}$ resonances.

5.5. Bifurcation scenario after the fold-flip bubble. The final slice of Figure 12(d) (slice f) is represented in Figure 13(f) for $\eta_3 = 0.7605$. In this case, there are no fold-flip bifurcations, and the 1:2 resonance $R^a_{1:2}$ is now connected to $R^{(2)b}_{1:1}$ by a Neimark–Sacker curve $NS^{(2)}$. Both Chenciner bifurcations CH and $CH^{(2)}$ remain close to $R^a_{1:2}$ and $R^{(2)b}_{1:1}$, respectively. The resulting scenario is similar to the one shown in Figure 10 for $\eta_3 = 0.757$, except that for $\eta_3 = 0.7605$ there is a fold-Neimark–Sacker bifurcation, and the normal form of the Hopf–Hopf bifurcation is S.III.

Finally, notice that the structure of codimension-two bifurcation curves in Figure 12 is reminiscent of the one associated to the branch NS_1 in the two-parameter analysis of Figure 5(c). Now it includes a fold on all of the bifurcations associated to this branch, induced by interactions with the fold curve generated by the generalized Hopf bifurcation GH. Therefore, instead of the Neimark–Sacker, the period-doubling bubble, and the cyclic-fold curves observed in the two-parameter analysis, a structure with a fold-Neimark–Sacker, a fold-flip bubble, and a pair of 1:1 strong resonance curves appears. In addition, adding a fold to $GPD^{a,b}$ and $R^{a,b}_{1:2}$, the points $P^{a,b}$ and $Q^{a,b}$ are obtained.

6. Degenerate 2:3 resonant Hopf–Hopf bifurcation $HH^0_{2:3}$ as the organizing center of the dynamics. For increasing values of α_2, the point HH^0 (where the generalized Hopf curve GH crosses the Hopf–Hopf bifurcation) approaches the 2:3 resonance $HH_{2:3}$. Thus, for $\alpha_2 \simeq 0.86$, GH crosses the curve HH at $HH_{2:3}$, leading to the codimension-four singularity $HH^0_{2:3}$. Then, for $\alpha_2 > 0.86$, the structure based on the fold-flip bubble FF described previously for $\alpha_2 = 0.83$ disappears. The resulting bifurcation scenario for $\alpha_2 = 0.89$ is shown in Figure 17, where the fold-flip bubble and the corresponding codimension-three bifurcation points $P^{a,b}$ and $Q^{a,b}$ do not exist. Nevertheless, the 2:3 resonant Hopf–Hopf bifurcation retains the codimension-two bifurcation curves $R^{a,b}_{1:2}$, $GPD^{a,b}$, and $R_{1:3}$.

Therefore, the fold-flip bubble FF and their codimension-three points $P^{a,b}$ and $Q^{a,b}$

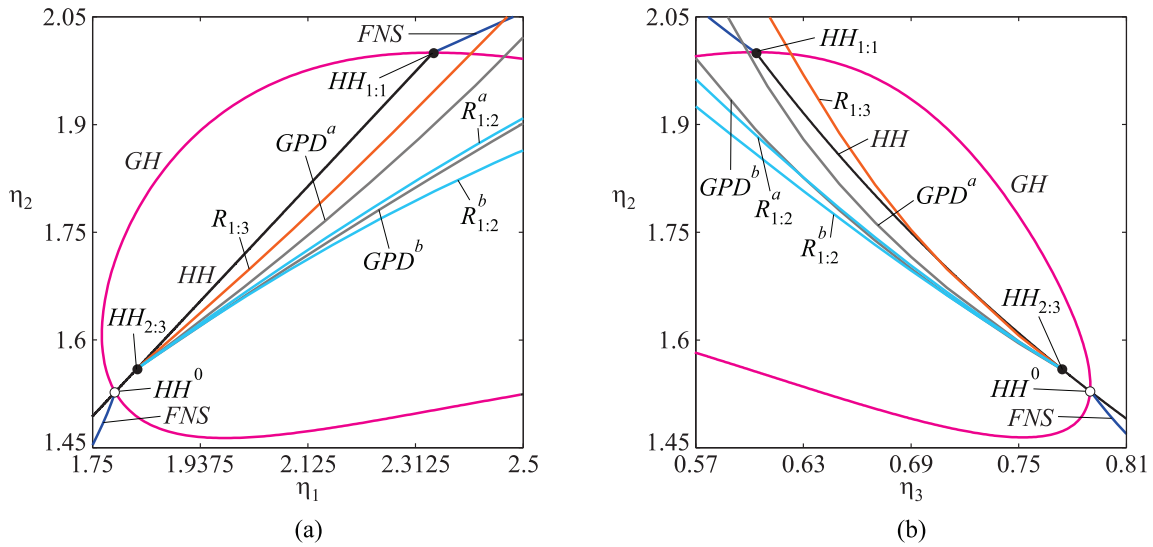

Figure 17. *Three-parameter bifurcation diagram for* $\alpha_2 = 0.89$.

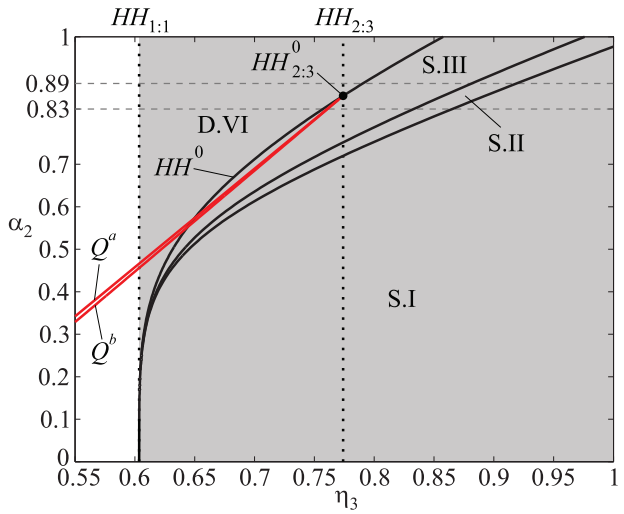

Figure 18. *Projection on the plane* $\eta_3 - \alpha_2$ *of the 4D continuation diagram varying* $(\eta_1, \eta_2, \eta_3, \alpha_2)$.

are organized around $HH^0_{2:3}$, at $(\eta_1, \eta_2, \eta_3, \alpha_2) \simeq (1.82714, 1.55957, 0.774002, 0.86)$. This is confirmed with the four-parameter $(\eta_1, \eta_2, \eta_3, \alpha_2)$ analysis, as shown in the projection of the continuation diagram on the plane $\eta_3 - \alpha_2$ in Figure 18. This figure includes the transition curves between the different unfoldings of the Hopf–Hopf bifurcation. They were obtained using the routines provided by Matcont (and derived in [17]) for computing numerically the normal form coefficients of the Hopf–Hopf bifurcation on the analytical curve (4) for different values of α_2. Figure 18 also includes the location of the 1:1 resonant Hopf–Hopf bifurcation (denoted by the dotted vertical line $HH_{1:1}$ for $\eta_3 \simeq 0.603553$) and the 2:3 resonance (denoted by the dotted vertical line $HH_{2:3}$ for $\eta_3 \simeq 0.774002$). The Hopf–Hopf bifurcation

occurs for values of $\eta_3 > 0.603553$ (gray zone in Figure 18), and sufficiently close to $HH_{1:1}$ the normal form is always D.VI. For α_2 small, the transitions occur almost simultaneously and the unfolding is practically S.I along the Hopf–Hopf bifurcation curve. As α_2 is increased, the cases S.II, S.III, and D.VI become distinguishable, as shown in Figure 2 for $\alpha_2 = 0.83$. Notice that the transition from the simple case S.III to the difficult one D.VI is determined by the curve HH^0. Finally, the codimension-three curves evolving from $HH^0_{2:3}$, as a result of the interaction between $HH_{2:3}$ and HH^0, are $Q^{a,b}$, while the ones corresponding to $P^{a,b}$ are not shown since they are very close to $Q^{a,b}$ and become indistinguishable.

7. Conclusions. In this paper the bifurcation structure related to a degenerate case of the 2:3 resonant Hopf–Hopf bifurcation has been studied. The nontrivial structure unfolded by this codimension-four bifurcation has been analyzed by means of numerical two- and three-parameter bifurcation diagrams. It has been shown that this singularity acts as an organizing center of the dynamics when the four-parameter space $(\eta_1, \eta_2, \eta_3, \alpha_2)$ is considered. The main phenomenon observed is the unfolding of a bifurcation structure involving a fold-flip bubble with two pairs of codimension-three bifurcation points. In one of these pairs, the fold-flip bifurcation interacts with a fold-Neimark–Sacker curve and a strong 1:2 resonance. At these points the nontrivial Floquet multipliers of the corresponding limit cycle are $(1, -1, -1)$. In the other pair the fold-flip bifurcation interacts with a generalized period-doubling bifurcation, generating a curve of 1:1 strong resonances of period-two cycles. This interaction between the involved codimension-two curves fold-flip, fold-Neimark–Sacker, generalized period-doubling, and 1:2 strong resonances has been described in detail. This analysis shows that not only the resonance of the Hopf–Hopf bifurcation is transferred to the Neimark–Sacker curves but also the vanishing of the first Lyapunov coefficient (by means of a cyclic-fold curve) is transferred to the resonant structure. Then, when a three-parameter space is considered, the original structure formed by the Neimark–Sacker, the period-doubling bubble, and the cyclic-fold curves is transformed into a similar structure involving fold-Neimark–Sacker, a fold-flip bubble, and a pair of 1:1 strong resonances (of period-two cycles). Moreover, this particular structure is generated from a single equilibrium point bifurcation: the degenerate 2:3 resonant Hopf–Hopf.

It is worth noting that the structure involving the fold-flip bubble and the four codimension-three points $P^{a,b}$ and $Q^{a,b}$ is mainly related to the Neimark–Sacker branch NS_1, i.e., the one exhibiting the couple of 1:2 strong resonances and the period-doubling bubble PD. In addition, the associated Hopf bifurcation branch H_1 presents the degenerate condition. Therefore, a similar structure could be observed when introducing a degenerate Hopf condition in the setting of the normal-internal k:2 resonance.

Appendix A. Defining conditions of the Hopf–Hopf bifurcation and its $p : q$ resonances. Let us transform the coupled system (2)–(3) into a dimensionless form by considering $\tau = \omega_{n_2} t$,

$$y_1'' - k_1 \left[1 - g(y_1')\right] y_1' + r^2 y_1 - k_{12} y_2' = 0, \tag{13}$$

$$y_2'' + k_2 y_2' + y_2 + y_1' = 0, \tag{14}$$

where the symbol $'$ means differentiation with respect to τ, $k_1 = \sigma_1/\omega_{n_2}$ and $k_2 = \sigma_2/\omega_{n_2}$ are the (linear) self-excitation and the damping coefficients of subsystems (13) and (14),

respectively, $g(y_1') = (-\alpha_2 y_1' + \alpha_3 y_1'^2)/\alpha_1$, $k_{12} = \sigma_{12}/\omega_{n_2}$, and $r = \omega_{n_1}/\omega_{n_2}$ is the ratio of natural frequencies of the uncoupled subsystems. The Jacobian associated to (13)–(14) at the equilibrium point $(x_1, x_1', y_1, y_1') = (0, 0, 0, 0)$ is

$$J = \begin{pmatrix} 0 & 1 & 0 & 0 \\ -r^2 & k_1 & 0 & k_{12} \\ 0 & 0 & 0 & 1 \\ 0 & -1 & -1 & -k_2 \end{pmatrix}, \tag{15}$$

and the associated characteristic polynomial results in

$$P(\lambda) = \lambda^4 + (k_2 - k_1)\,\lambda^3 + \left(1 + r^2 + k_{12} - k_1 k_2\right)\lambda^2 + \left(r^2 k_2 - k_1\right)\lambda + r^2. \tag{16}$$

The necessary conditions to have a Hopf–Hopf bifurcation, i.e., two pairs of eigenvalues on the imaginary axis, are

$$k_1 = k_2, \tag{17}$$

$$r = 1, \tag{18}$$

$$k_1 k_2 < k_{12}, \tag{19}$$

i.e., the linear self-excitation coefficient and the natural frequency of subsystem (13) must be equal to the value of the damping coefficient and the natural frequency of subsystem (14), respectively, and the coupling coefficient must be greater than the product of the damping coefficients. The characteristic polynomial on the Hopf–Hopf condition results in

$$P(\lambda) = \lambda^4 + 2\Delta\lambda^2 + 1, \tag{20}$$

where $\Delta = \left(2 - k_1^2 + k_{12}\right)/2$. The roots are $\lambda_{1\pm} = \pm i\bar{\omega}_1$ and $\lambda_{2\pm} = \pm i\bar{\omega}_2$, where

$$\bar{\omega}_{1,2} = \sqrt{\Delta \mp \sqrt{\Delta^2 - 1}} \tag{21}$$

are the normalized frequencies of both Hopf bifurcation branches.

The frequency ratio on the Hopf–Hopf condition results in

$$\frac{\bar{\omega}_1}{\bar{\omega}_2} = \Delta - \sqrt{\Delta^2 - 1}, \tag{22}$$

and the condition leading to a $p : q$ resonance is

$$\Delta = \Delta^{p:q} = \frac{p^2 + q^2}{2pq}, \tag{23}$$

leading to the normalized frequencies at the $p : q$ resonant Hopf–Hopf bifurcation

$$\bar{\omega}_1 = \sqrt{p/q}, \quad \bar{\omega}_2 = \sqrt{q/p}, \tag{24}$$

which do not depend on the parameters.

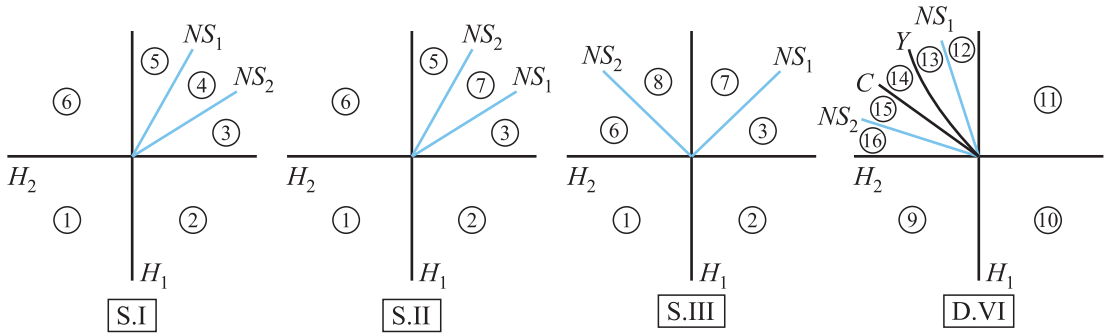

Figure 19. *Unfoldings of the Hopf–Hopf bifurcation for the four cases detected in this paper.*

Appendix B. Hopf–Hopf bifurcation normal form and local unfoldings observed in this paper. The truncated normal form of the Hopf–Hopf bifurcation in polar coordinates is given by [18]

$$\dot{r}_1 = r_1\left(\mu_1 + p_{11}r_1^2 + p_{12}r_2^2 + s_1 r_2^4\right), \tag{25}$$

$$\dot{r}_2 = r_2\left(\mu_2 + p_{21}r_1^2 + p_{22}r_2^2 + s_2 r_1^4\right), \tag{26}$$

$$\dot{\varphi}_1 = \omega_1, \tag{27}$$

$$\dot{\varphi}_2 = \omega_2, \tag{28}$$

where r_i, φ_i, and ω_i, $i = 1, 2$, are the amplitudes, phases, and frequencies of the orbits, respectively, $\mu_{1,2}$ are bifurcation parameters, and p_{jk} and s_k, $j, k = 1, 2$, are real coefficients. Since the amplitudes and phases in the truncated normal form are decoupled, the dynamics can be reproduced by the amplitude system (25)–(26). Depending on the signs of p_{11} and p_{22}, two different scenarios arise: the "simple" ones when $p_{11} \times p_{22} > 0$, and the "difficult" ones when $p_{11} \times p_{22} < 0$. Considering the variables $\xi_1 = \mp p_{11}r_1^2$ and $\xi_2 = -p_{22}r_2^2$, and rescaling time, the amplitude system can be expressed as

$$\dot{\xi}_1 = \xi_1\left(\mu_1 \mp \xi_1 - \theta\xi_2 + \Theta\xi_2^2\right), \tag{29}$$

$$\dot{\xi}_2 = \xi_2\left(\mu_2 \mp \delta\xi_1 + \xi_2 + \Delta\xi_1^2\right), \tag{30}$$

where the sign "−" corresponds to the simple cases (with $p_{11} < 0$ and $p_{22} < 0$) and the sign "+" to the difficult cases (with $p_{11} > 0$ and $p_{22} < 0$), $\theta = p_{12}/p_{22}$, $\delta = p_{21}/p_{11}$, $\Theta = s_1/p_{22}^2$, and $\Delta = s_2/p_{22}^2$.

The two-parameter unfolding corresponding to the four cases detected in the present paper, namely S.I ($\theta > 0$, $\delta > 0$, $\theta \times \theta > 1$), S.II ($\theta > 0$, $\delta > 0$, $\theta \times \theta < 1$), S.III ($\theta > 0$, $\delta < 0$), and D.VI ($\theta > 0$, $\delta < 0$), are depicted in Figure 19. The generic phase portraits are shown in Figure 20. The dot at the origin represents the equilibrium point of the system, the dot in the horizontal axis represents the cycle associated to the Hopf bifurcation H_1, and the dot in the vertical axis represents the cycle associated to H_2. The dot located out of the axes represents the 2D torus, and the limit cycle corresponds to the 3D torus. Notice that the unfoldings depicted in Figure 19 but rotated clockwise 135° coincide with the local unfoldings observed near the nonresonant Hopf–Hopf bifurcation point in the parameter plane $\eta_1 - \eta_2$ for η_3 fixed.

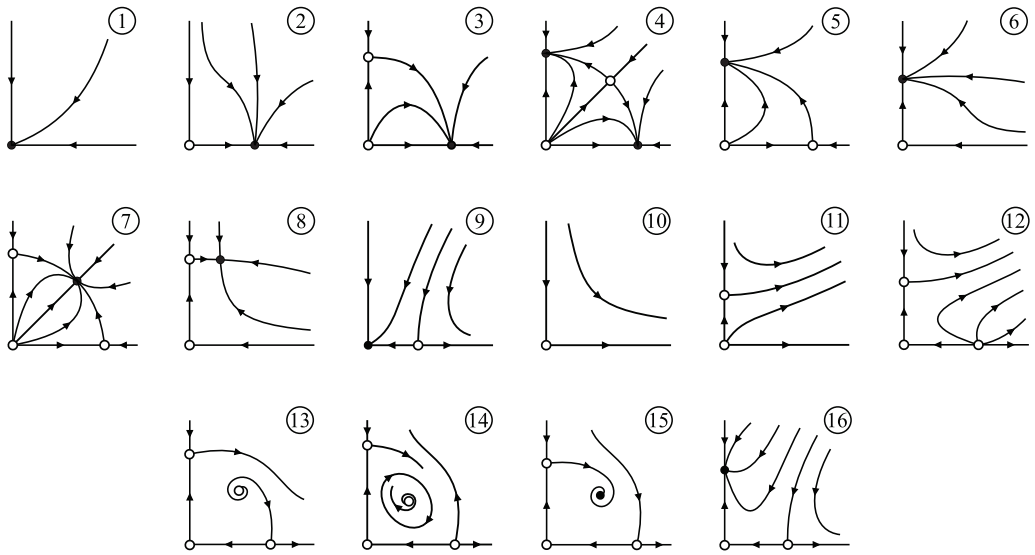

Figure 20. *Generic phase portraits corresponding to the unfoldings shown in Figure 19.*

Appendix C. Dynamics associated to the nonresonant and resonant Hopf–Hopf bifurcation. The dynamics associated to the two-parameter bifurcation diagrams for $\eta_3 = 0.778$ and $\eta_3 = 0.77$ (Figures 3 and 5, respectively) described in section 3 is illustrated in Figures 21 and 22 by the largest Lyapunov exponent corresponding to the stable solutions. Numerical simulations with the initial condition $(x_1, x_2, x_3, x_4) = (0.0001, 0, 0, 0)$ and parameter values (η_1, η_2) on a grid of 600×600 equally spaced points (in both diagrams and the blow-up in Figure 22b) were performed. The first 30×10^4 s of the simulation were discarded, and the time series composed by the following 25×10^4 s were used to compute all the Lyapunov exponents using the algorithm described in [34] and implemented in [13]. The results in Figures 21 and 22 present a rough picture of the complex dynamics introduced by the resonant bifurcation structure since, to display the largest Lyapunov exponent, those sufficiently close to zero were discarded, introducing an uncertainty near bifurcation curves. In addition, near the period-two bubble the transients are extremely large, and the time series discarded and used to compute the exponents should be more than two orders of magnitude larger, and therefore the corresponding blow-up is not shown. The grayscale region corresponds to the largest Lyapunov exponent of the stable equilibrium point (all the exponents are negative), the blue-green regions (one exponent is zero) correspond to the largest exponent of a stable periodic orbit, and the red-yellow region (two exponents are zero) corresponds to quasi-periodic orbits. In all of the cases, brighter colors mean closest to zero values as is denoted by the scales in Figure 21 (right). The white region corresponds to a stable limit cycle not directly associated to the nondegenerate Hopf–Hopf bifurcation.

In Figure 21, the limit cycle in the region delimited by CF and H_1-NS_1^a is the one associated to H_1, that born towards the left (see the unfoldings and phase portraits corresponding to the normal form S.III in Figures 19 and 20). The cycle arises stable in the upper segment of H_1 (above HH) and unstable in the bottom segment (below HH), but it becomes stable

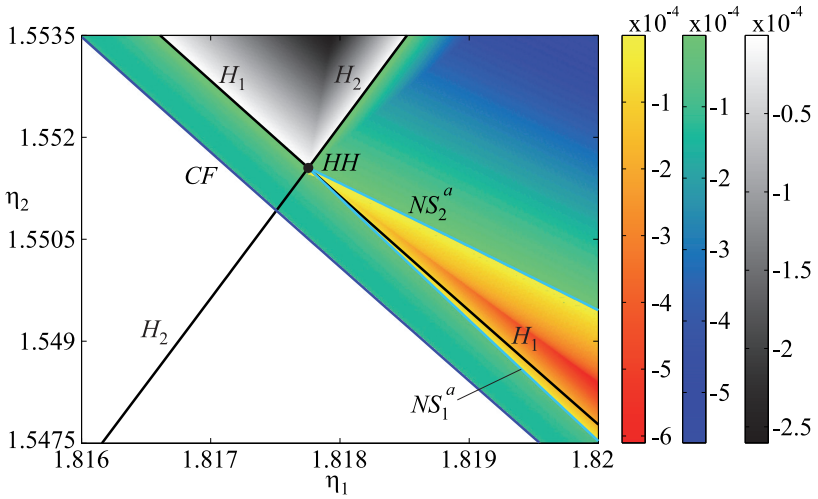

Figure 21. *Largest Lyapunov exponent for* $\alpha_2 = 0.83$ *and* $\eta_3 = 0.778$. *Equilibrium point: grayscale. Limit cycles: blue to green. Quasi-periodic solutions: red to yellow.*

at NS_1^a. On the other hand, the cycle born at H_2 exists on the right. It is stable in the upper segment and unstable in the lower one (below HH). As expected, the quasi-periodic orbit exists between NS_1^a and NS_2^a.

In the case of Figure 22, parameter $\eta_3 = 0.77$, and thus the bifurcation structure arising in $HH_{2:3}$, introduces additional dynamical phenomena on the quasi-periodic orbit, as shown in the blow-up of Figure 22(b).

Appendix D. Normal forms of some codimension-two bifurcations and values of their coefficients for key bifurcations. For the sake of completeness, the canonical unfoldings of the truncated normal form of those codimension-two bifurcations appearing in Table 5 are listed below. These equations (with unfolding parameters $\beta_{1,2}$) approximate the second iterate of the Poincaré map associated to the critical limit cycle (see [6, 8]).

Generalized period-doubling bifurcation (section 2.1.2 of [6]):

$$\dot{\xi} = \beta_1 \xi + \beta_2 \xi^3 + e\xi^5.$$

Neimark–Sacker 1:2 *strong resonance* (section 2.2.3 of [6]):

$$\begin{aligned} \dot{\xi_1} &= \xi_2, \\ \dot{\xi_2} &= \beta_1 \xi_1 + \beta_2 \xi_2 + a\xi_1^3 + b\xi_1^2 \xi_2. \end{aligned}$$

Fold-flip bifurcation (section 2.1.6 of [6]):

$$\begin{aligned} \dot{\xi_1} &= \beta_1 + \beta_2 \xi_1 + a_{20}\xi_1^2 + a_{02}\xi_2^2 + (a_{30} + a_{20})\,\xi_1^3 + (a_{12} + a_{02})\,\xi_1 \xi_2^2, \\ \dot{\xi_2} &= b_{11}\xi_1 \xi_2 + (b_{21} + b_{11})\,\xi_1^2 \xi_2 + b_{03}\xi_2^3. \end{aligned}$$

Fold-Neimark–Sacker bifurcation (section 2.2.1 of [8]):

$$\begin{aligned} \dot{\xi_1} &= \beta_1 + \xi_1^2 + s\,|\xi_2|^2, \\ \dot{\xi_2} &= (\beta_2 + i\omega_1)\,\xi_2 + (\theta + i\upsilon)\,\xi_1 \xi_2 + \xi_1^2 \xi_2. \end{aligned}$$

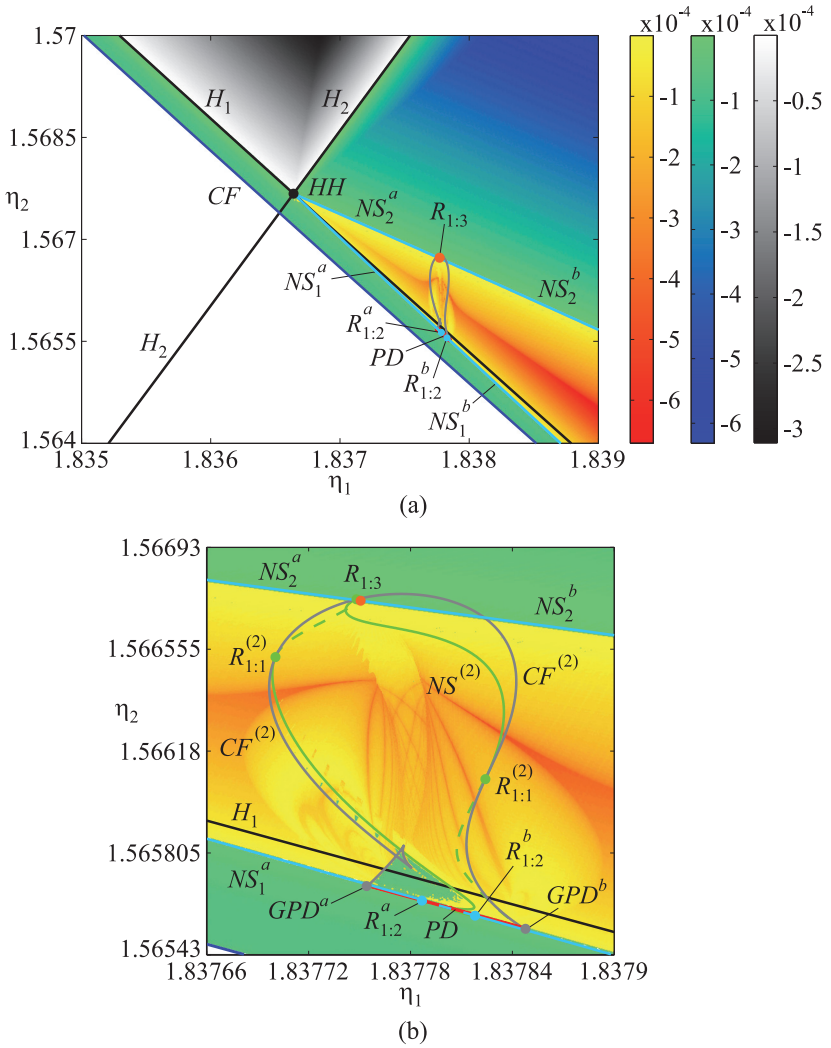

Figure 22. *Largest Lyapunov exponent for* $\alpha_2 = 0.83$ *and* $\eta_3 = 0.77$. *Equilibrium point: grayscale. Limit cycles: blue to green. Quasi-periodic solutions: red to yellow.*

Acknowledgments. The authors would like to thank the Associate Editor and the anonymous reviewers for their helpful comments and suggestions.

REFERENCES

[1] Abadi, *On self-excited auto-parametric systems*, Nonlinear Dynamics, 24 (2001), pp. 147–166.
[2] C. Baesens and R. S. MacKay, *Resonances for weak coupling of the unfolding of a saddle-node periodic orbit with an oscillator*, Nonlinearity, 20 (2007), pp. 1283–1298.
[3] T. Bakri and F. Verhulst, *Bifurcations of quasi-periodic dynamics: Torus breakdown*, Z. Angew. Math. Phys., 65 (2014), pp. 1053–1076.
[4] H. W. Broer, V. Naudot, R. Roussarie, K. Saleh, and F. O. O. Wagener, *Organising centres in the semi-global analysis of dynamical systems*, Int. J. Appl. Math. Stat., 12 (2007), pp. 7–36.

[5] H. W. Broer, R. van Dijk, and R. Vitolo, *Survey of strong normal-internal k:l resonances in quasi-periodically driven oscillators for* $l = 1, 2, 3$, in Proceedings of the International Conference on SPT (Otranto, Italy), G. Gaeta, R. Vitolo, and S. Walcher, eds., World Scientific, Singapore, 2007, pp. 45–55.

[6] V. De Witte, F. Della Rossa, W. Govaerts, and Yu. A. Kuznetsov, *Numerical periodic normalization for codim* 2 *bifurcations of limit cycles: Computational formulas, numerical implementation, and examples*, SIAM J. Appl. Dyn. Syst., 12 (2013), pp. 722–788.

[7] V. De Witte, W. Govaerts, Yu. A. Kuznetsov, and H. G. E. Meijer, *Numerical Periodic Normalization for codim* 2 *Bifurcations of Limit Cycles with Center Manifold of Dimension Higher than* 3, preprint, arXiv:1210.6205v1 [math.DS], 2012.

[8] V. De Witte, W. Govaerts, Yu. A. Kuznetsov, and H. G. E. Meijer, *Analysis of bifurcations of limit cycles with Lyapunov exponents and numerical normal forms*, Phys. D, 269 (2014), pp. 126–141.

[9] A. Dhooge, W. Govaerts, and Yu. A. Kuznetsov, *MATCONT: A MATLAB package for numerical bifurcation analysis of ODEs*, ACM Trans. Math. Software, 29 (2003), pp. 141–164.

[10] A. Dhooge, W. Govaerts, Yu. A. Kuznetsov, H. G. E. Meijer, and B. Sautois, *New features of the software Matcont for bifurcation analysis of dynamical systems*, Math. Comput. Model. Dyn. Syst., 14 (2008), pp. 147–175.

[11] V. S. Gonchenko, I. I. Ovsyannikov, C. Simó, and D. Turaev, *Three-dimensional Hénon-like maps and wild Lorenz-like attractors*, Internat. J. Bifur. Chaos Appl. Sci. Engrg., 15 (2005), pp. 3493–3508.

[12] W. Govaerts, J. Guckenheimer, and A. Khibnik, *Defining functions for multiple Hopf bifurcations*, SIAM J. Numer. Anal., 34 (1997), pp. 1269–1288.

[13] V. Govorukhin, *Calculation Lyapunov Exponents for ODE,* open source MATLAB code, 2004. http://www.mathworks.com/matlabcentral/fileexchange/4628-calculation-lyapunov-exponents-for-ode.

[14] A. I. Khibnik, Y. A. Kuznetsov, V. V. Levitin, and E. V. Nikolaev, *Continuation techniques and iterative software for bifurcation analysis of ODEs and iterated maps*, Phys. D, 62 (1993), pp. 360–361.

[15] P. M. Kitanov, W. F. Langford, and A. R. Willms, *Double Hopf bifurcation with Huygens symmetry*, SIAM J. Appl. Dyn. Syst., 12 (2013), pp. 126–174.

[16] E. Knobloch and M. R. E. Proctor, *The double Hopf bifurcation with* 2:1 *resonance*, Proc. Roy. Soc. Lond. Ser. A, 415 (1988), pp. 61–90.

[17] Yu. A. Kuznetsov, *Numerical normalization techniques for all codim* 2 *bifurcations of equilibria in ODE's*, SIAM J. Numer. Anal., 36 (1999), pp. 1104–1124.

[18] Yu. A. Kuznetsov, *Elements of Applied Bifurcation Theory*, 3rd ed., Springer-Verlag, New York, 2004.

[19] W. F. Langford and K. Zhan, *Interactions of Andronov-Hopf and Bogdanov-Takens bifurcations*, in The Arnoldfest (Toronto, ON, 1997), Fields Inst. Commun. 24, Amer. Math. Soc., Providence, RI, 1999, pp. 365–383.

[20] V. G. LeBlanc, *On some secondary bifurcations near resonant Hopf-Hopf interactions*, Dyn. Contin. Discret. Impuls. Syst., 7 (2000), pp. 405–427.

[21] V. G. LeBlanc and W. F. Langford, *Classification and unfoldings of* 1:2 *resonant Hopf bifurcation*, Arch. Ration. Mech. Anal., 136 (1996), pp. 305–357.

[22] A. I. Mees and L. O. Chua, *The Hopf bifurcation theorem and its applications to nonlinear oscillations in circuits and systems*, IEEE Trans. Circuits Syst. I, 26 (1979), pp. 235–254.

[23] J. L. Moiola and G. Chen, *Hopf Bifurcation Analysis: A Frequency Domain Approach*, Nonlinear Sci. Ser. 21, World Scientific, Singapore, 1996.

[24] L. Pust and A. Tondl, *System with a non-linear negative self-excitation*, Internat. J. Nonlinear Mech., 43 (2008), pp. 497–503.

[25] G. Revel, D. M. Alonso, and J. L. Moiola, *Interactions between oscillatory modes near a* $2:3$ *resonant Hopf-Hopf bifurcation*, Chaos, 20 (2010), 043106.

[26] G. Revel, D. M. Alonso, and J. L. Moiola, *Numerical semi-global analysis of a* $1:2$ *resonant Hopf-Hopf bifurcation*, Phys. D, 247 (2013), pp. 40–53.

[27] K. Saleh and F. O. O. Wagener, *Semi-global analysis of periodic and quasi-periodic normal-internal* k:1 *and* k:2 *resonances*, Nonlinearity, 23 (2010), pp. 2219–2252.

[28] A. L. Shilnikov, L. P. Shilnikov, and D. V. Turaev, *Normal forms and Lorenz attractors*, Internat. J. Bifur. Chaos Appl. Sci. Engrg., 3 (1993), pp. 1123–1139.

[29] N. Sri Namachchivaya, M. M. Doyle, W. F. Langford, and N. W. Evans, *Normal form for generalized Hopf bifurcation with non-semisimple* 1:1 *resonance*, Z. Angew. Math. Phys., 45 (1994), pp. 312–335.

[30] F. Takens and F. O. O. Wagener, *Resonances in skew and reducible quasi-periodic Hopf bifurcations*, Nonlinearity, 13 (2000), pp. 377–396.

[31] S. A. Van Gils, M. Krupa, and W. F. Langford, *Hopf bifurcation with non-semisimple* 1:1 *resonance*, Nonlinearity, 3 (1990), pp. 825–850.

[32] R. Vitolo, H. Broer, and C. Simó, *Routes to chaos in the Hopf-saddle-node bifurcation for fixed points of* 3*D-diffeomorphisms*, Nonlinearity, 23 (2010), pp. 1919–1947.

[33] J. Warminski, *Nonlinear normal modes of coupled self-excited oscillators in regular and chaotic vibration regimes*, J. Theoret. Appl. Mech., 46 (2008), pp. 693–714.

[34] A. Wolf, J. B. Swift, H. L. Swinney, and J. A. Vastano, *Determining Lyapunov exponents from time series*, Phys. D, 16 (1985), pp. 285–317.